

Geometric Parameter Analysis of H-Darrieus Wind Turbines Based on 3D CFD

Kazuteru Fukushima

A thesis in
The Department of
Mechanical, Industrial & Aerospace Engineering

Presented in Partial Fulfillment of the Requirements
for the Degree of Master of Applied Science (Mechanical Engineering) at
Concordia University
Montreal, Quebec, Canada

November 2021

© Kazuteru Fukushima, 2021

CONCORDIA UNIVERSITY

School of Graduate Studies

This is to certify that the thesis prepared

By: Kazuteru Fukushima

Entitled: Geometric Parameter Analysis of H-Darrieus Wind Turbines Based on 3D CFD

and submitted in partial fulfillment of the requirements for the degree of

Master of Applied Science (Mechanical Engineering)

complies with the regulations of the University and meets the accepted standards with respect to originality and quality.

Signed by the final Examining Committee:

_____ Chair

Carole El Ayoubi

_____ Examiner

Carole El Ayoubi

_____ Examiner

Bruno Lee

_____ Supervisor

Marius Paraschivoiu

Approved by _____

Dr. Sivakumar Narayanswamy, Chair of Department of Graduate Program Director

December 15, 2021

Dr. Mourad Debbabi, Dean of Faculty

Abstract

Geometric Parameter Analysis of H-Darrieus Wind Turbines Based on 3D CFD

Kazuteru Fukushima

The performance prediction of straight bladed vertical axis wind turbines is always of interest in the wind power generation industry. Computational Fluid Dynamic (CFD) is performed to explore the geometric design space, such as a turbine diameter, a blade length, and a wing section. The objective is to relate these design parameters to the maximum power coefficient of the H-type Darrieus vertical axis wind turbine. This analysis is based on data already available in the literature complemented by additional CFD runs to enhance the number of turbines investigated. By analyzing these results, two main geometric parameters, the blade thickness and large aspect ratio, are identified as the main parameters that affect the turbine's power coefficient. This confirms the importance of the blade geometry in the performance of vertical axis wind turbines. Furthermore, some model equations are proposed to predict a power coefficient without any large simulations. The suggested model equations can roughly predict the power coefficients; moreover, it can quantify the effect of the blade thickness and the blade aspect ratio.

Acknowledgments

I would like to thank Dr. Marius Paraschivoiu for his immeasurable support, guidance, and insight. His passionate and skillful support always encouraged my research and improved not only the quality but also originality. Also, I would like to express my thanks to the continuous and flexible support in the difficult situation. There is no doubt that one could not wish for a better supervisor.

I would like to thank the Engineering and Computer Science in Concordia university for the financial support through Concordia International Tuition Award of Excellence, along with its staff.

My thanks go to Maryam Zabarjad Shiraz, Belabes Belkacem, and Farshad Rezaei for their advice, their suggestions, and contributing to precious working environment during my research. I also appreciate I could work with you.

I am also sincerely grateful to Anahita Ghassemi Panah, Marc Alexandre Allard, Ahmed Hammad, and Hadis Montazerinejad for their friendship and support.

I would like to thank Metropolitan expressway company ltd., for giving a great opportunity to study as a graduate student and a lot of financial support. It is essential for this thesis and my fruitful research.

Lastly, I would like to thank my loving family, Miki Fukushima, Iori Fukushima, and Yoneko Fukushima for their grateful love and support at my most challenging times.

Table of Contents

List of Figures	vii
List of Tables.....	ix
List of Abbreviations.....	x
1 Introduction	1
1.1 Social background	1
1.2 Technological background	1
1.3 Quantities of interest associated with Wind Turbines	3
1.3.1 Solidity	3
1.3.2 Aspect ratio	4
1.4 Motivation of this thesis	4
1.5 Overview of the Literature associated with CFD for VAWT	5
1.6 Objectives	6
2 VAWT parametric study	7
2.1 Maximum Power Coefficient (MaxCP) relationship to single key parameters.....	7
2.1.1 Maximum power coefficient vs Solidity.....	8
2.1.2 TSR for the maximum power coefficient vs Solidity	10
2.1.3 Maximum power coefficient vs number of blades.....	10
2.1.4 Maximum power coefficient vs aspect ratio	11
2.1.5 Maximum power coefficient vs ratio of wing thickness to chord.....	13
2.1.6 Maximum power coefficient vs projected area	14
2.1.7 Difference of turbulence model.....	15
2.1.8 Coefficient of determination between MaxCP and parameters	15
2.1.9 Summary of the analysis between MaxCP and single parameters.....	16
2.2 Maximum Power Coefficient (MaxCP) relationship to combinations of factors.....	17
2.2.1 Combination of solidity and area	17
2.2.2 Combination of Area and Solidity	18
2.2.3 Combination of area and aspect ratio	18
2.2.4 Combination of blade thickness and aspect ratio	19
2.2.5 Summary of the analysis between MaxCP and combinations of parameters	21
3 CFD simulations.....	22
3.1 Govern equations and simulation software	22

3.2	Segregated Flow Solver.....	22
3.2.1	SIMPLE method.....	23
3.2.2	RANS	23
3.2.3	<i>SST k – ω</i>	24
3.2.4	Implicit method setup.....	25
3.3	Geometry overview	26
3.3.1	Geometry.....	26
3.3.2	Boundary conditions	29
3.3.3	Meshing.....	31
3.3.4	Cases.....	34
3.3.5	Coordinates definition	39
3.3.6	Summary of geometry	40
4	CFD Result.....	41
4.1	Vorticity.....	45
4.2	Comparison to the original power coefficient	48
5	Data analysis and proposed models	49
5.1	Least squares method.....	49
5.2	t-test	49
5.3	t-distribution and p-value.....	50
5.4	Single parameter model function.....	50
5.5	Multiple parameters model functions	54
5.5.1	Result.....	54
5.6	Findings for model functions.....	57
6	Conclusion.....	58
6.1	Summary.....	58
6.2	Future work.....	58
7	References	60

List of Figures

Figure 1 Type of wind turbine.....	2
Figure 2 Different kinds of VAWTs	2
Figure 3 The number of papers about VAWT, 3D, CFD.....	6
Figure 4 Case study steps	6
Figure 5 Maximum power coefficient vs Solidity	8
Figure 6 Maximum power coefficient without shaft or arms vs Solidity	9
Figure 7 Maximum power coefficient without shaft or arms with sst k-omega vs Solidity	9
Figure 8 TSR for the maximum power coefficient vs Solidity	10
Figure 9 Maximum power coefficient vs number of blades	11
Figure 10 Maximum power coefficient vs aspect ratio	12
Figure 11 Maximum power coefficient without shaft or arms with sst k-omega vs Aspect ratio ..	12
Figure 12 Maximum power coefficient vs ratio of wing thickness to chord	13
Figure 13 Maximum power coefficient without shaft or arms with sst k-omega turbulence model	13
Figure 14 Maximum power coefficient vs Area	14
Figure 15 Maximum power coefficient without shaft or arms with sst k-omega vs Area	14
Figure 16 Combination of Solidity and Aspect ratio	17
Figure 17 Combination of area and solidity	18
Figure 18 Combination of area and aspect ratio	19
Figure 19 Combination of blade thickness and aspect ratio.....	20
Figure 20 Combination of blade thickness and Aspect ratio without shaft and arms	20
Figure 21 Type of turbulence model	23
Figure 22 Computational domain and rotational region	26
Figure 23 Rotational domain top view	27
Figure 24 Rotational domain side view.....	28
Figure 25 Symmetrical plane	29
Figure 26 The position of inlet and outlet boundaries	30
Figure 27 Open boundary conditions	31
Figure 28 Mesh around the blade	32
Figure 29 Rotating domain.....	32
Figure 30 Vertical plane	33
Figure 31 Prism layer	33
Figure 32 Mesh around the leading edge (Left:0.004m Right:0.008m).....	35
Figure 33 Case A mesh	35
Figure 34 Case B mesh.....	36
Figure 35 Case C mesh.....	36
Figure 36 Case D mesh	37
Figure 37 Case E mesh.....	37
Figure 38 Case F mesh	38
Figure 39 Coordinate system.....	39
Figure 40 Summary of geometry	40
Figure 41 Result of power coefficient.....	41

Figure 42 Power coefficient in case A42

Figure 43 Power coefficient in case B42

Figure 44 Power coefficient in case C43

Figure 45 Power coefficient in case D43

Figure 46 Power coefficient in case E.....44

Figure 47 Power coefficient in case F.....44

Figure 48 Case A vorticity rotation region.....45

Figure 49 Case B vorticity rotation region.....45

Figure 50 Case C vorticity rotation region.....46

Figure 51 Case D vorticity rotation region.....46

Figure 52 Case E vorticity rotation region47

Figure 53 Case F vorticity rotation region47

Figure 54 t-test procedure50

Figure 55 Fit function of the blade thickness52

Figure 56 Fit function of aspect ratio53

Figure 57 Candidate 1 model equation plane.....56

Figure 58 Candidate 2 model equation plane.....56

Figure 59 Candidate 3 model equation plane.....56

List of Tables

Table 1 Cases	7
Table 2 Comparison for the number of blades with almost the same solidity cases.....	11
Table 3 Cp for different turbulence models	15
Table 4 Coefficient of determination between MaxCP and parameters	15
Table 5 Inlet boundary condition	29
Table 6 Outlet boundary condition.....	30
Table 7 Employed Cases	34
Table 8 Number of cells	34
Table 9 Simulation result	41
Table 10 Power coefficient comparison between my simulation and the published values	48
Table 11 Training cases.....	51
Table 12 Validation cases	51
Table 13 Trend line functions for blade thickness	52
Table 14 Trend line functions for aspect ratio	53
Table 15 Result of multiple regression	55
Table 16 Prediction results	55

List of Abbreviations

Abbreviation

3D:Three-dimensional.....	6
CFL: Courant-Friedrichs-Lewy.....	25
HAWT:Horizontal axis vertical axis wind turbine	1
IDDES:Improved delayed detached eddy simulation	7
LES:Large eddy simulation.....	7
RANS: Reynolds-Averaged Navier-Stokes	23
RNG:Re-normalization group.....	7
SIMPLE: Semi-implicit method for pressure-linked equation	23
SST:Shear stress transport	24, 34
TSR: Tip-speed ratio	3
VAWT:Vertical axis wind turbine	1

1 Introduction

1.1 Social background

In 1992, Kyoto protocol to the United Nations Framework Convention on Climate Change was adopted, and a many of counties have discussed and ratified it. Although the United States were not in favor of ratification it led to the 2015 United Nations Climate Change Conference which was held in Paris. For all practical purposes, almost every country decided to target the goal to decrease the CO₂ emission and increase research the renewable energy.

Wind power generation is still required to increase, and the performance improvement is also a worthy task in the world. Temporarily reduced energy demand due to COVID-19 is still higher than the renewable energy supply [1] [2]. Windmill can extract potential energy from air during the day or night when the wind blows. The most important fact is that power can be generated regardless of the daytime as long as the wind flows. Also, it does not exhaust any radioactive substances. The wind energy extraction is now very popular because it can produce a lot of energy without dangerous emissions and the instability of material cost.

1.2 Technological background

Wind power generation has two types of systems; horizontal axis wind turbine and vertical axis wind turbines (HAWT and VAWT) as shown in Figure 1. HAWTs are well developed in the renewable energy industry. These propeller wind turbines have a relatively high maximum power coefficient, and they are installed everywhere in the world. However, they need to accompany yaw function machines and make noise. Moreover, these turbines have a wind-direction dependency, so that it is hard to continually generate energy in the places where the wind direction changes significantly.

On the other hand, VAWTs have two positive aspects from a technological viewpoint. First, VAWTs don't require yaw motion. These turbines are independent of wind direction and can operate in the sudden wind direction changing situation. Second, the operating tip-speed ratio can be smaller than HAWT in the rated situation. Furthermore, the shape of blades also decreases the wind noises. VAWTs seem to have a lot of advantages; however, the power coefficient is still lower than HAWT.

This thesis focuses on H-Darrieus wind turbine. H-Darrieus wind turbine has a relatively simple blade geometry as shown in Figure 2 [3]. It is advantageous for both the initial and the running cost. Moreover, it has relatively high-power coefficient, so wind-farming has a possibility to generate a huge amount of electric energy. H-darrieus wind turbine has been studied theoretically and experimentally with the goal of providing accurate power predictions. The results of these works are typically presented in term of power coefficient. More recently, computational fluid dynamics (CFD) has been extensively used. CFD is a well-developed simulation tool; however, there are still arguable points for power prediction of VAWT.

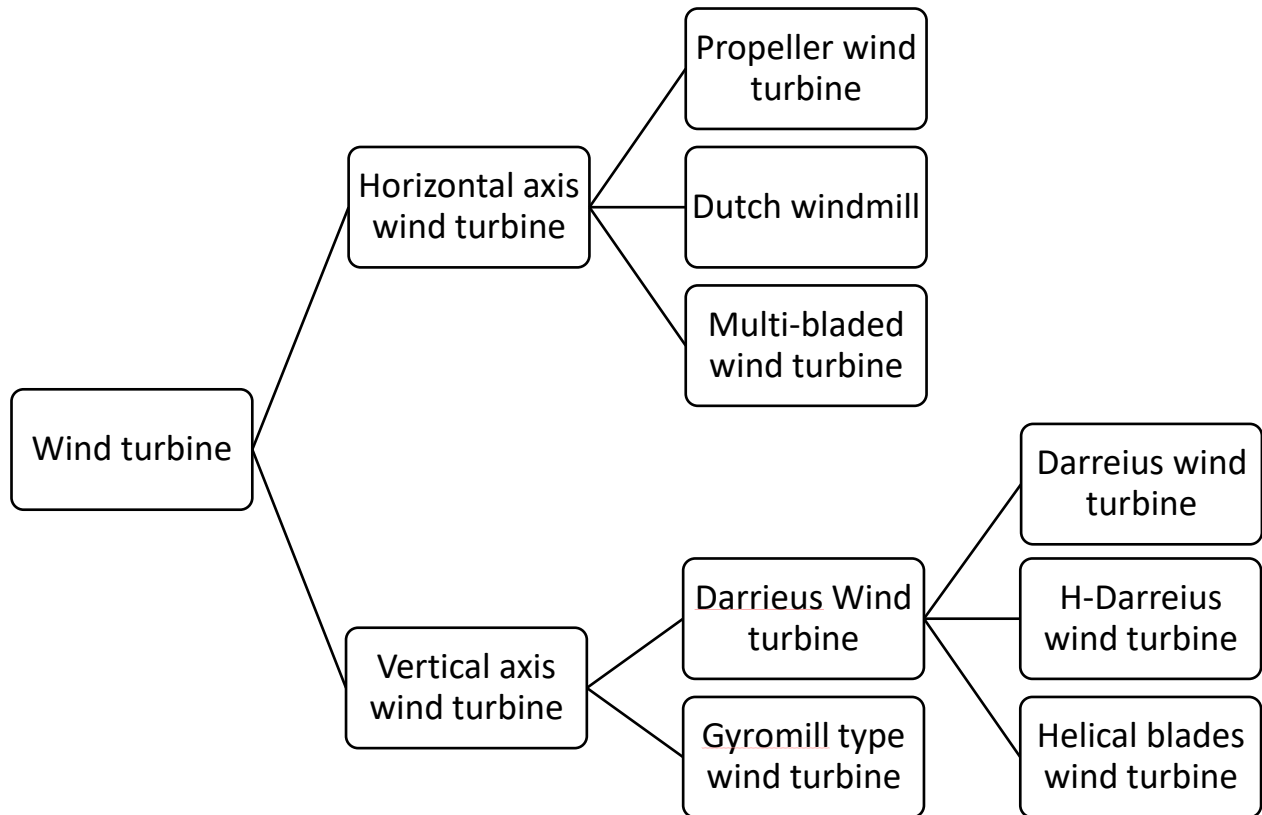


Figure 1 Type of wind turbine

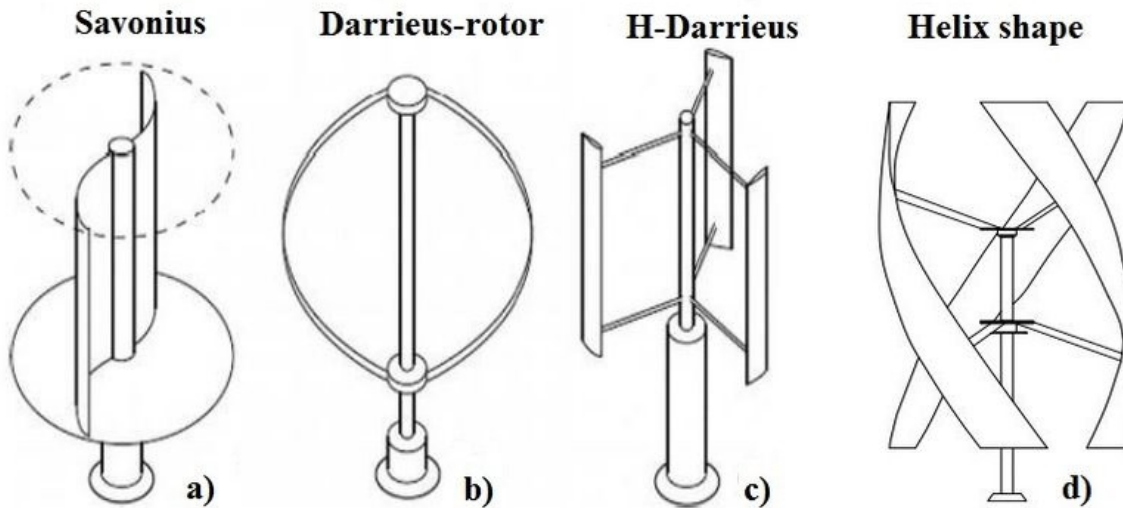


Figure 2 Different kinds of VAWTs

1.3 Quantities of interest associated with Wind Turbines

Wind power generation changes air kinetic energy into electrical power through by generating torque. Assuming a constant density, the air energy is the third power to the wind velocity as shown in (1.1) and (1.2),

$$P_{air} = \frac{1}{2} \rho A U^3 \quad (1.1)$$

$$A = DL \quad (1.2)$$

where P_{air} [kg m²/s³] is air energy, ρ [kg/m³] is a density, A [m²] is the projected area, U [m/s] is a free stream velocity, D [m] is the rotational diameter, and L [m] is the blade length.

The Tip-speed ratio (TSR) is introduced to define a non-dimensional number related to velocity and rotation. TSR is the ratio of the free stream velocity to the blade speed as shown in (1.3),

$$\lambda = \frac{V}{U} = \frac{R\Omega}{U} = \frac{D\Omega}{2U} \quad (1.3)$$

where λ [-] is tip-speed ratio, V [m/s] is the blade velocity, R [m] is a rotational radius, and Ω [1/s] is the rotational speed.

As discussed in the past section, the power coefficient is the most relevant variable to the turbine's performance. The power coefficient is defined as shown in (5.9)(1.3),

$$P = C_p P_{air} = \frac{1}{2} C_p \rho A U^3 \quad (1.4)$$

where P [kg m²/s³] is the power that the turbine generated, and C_p [-] is the power coefficient. The power coefficient indicates how much turbine can extract power from the air potential energy. Also, the power coefficient has a theoretical limit called Betz-Joukowsky limit [4]. The maximum power coefficient should be less than 0.592.

1.3.1 Solidity

Solidity is the ratio of the rotational diameter to the total blades' length. It is defined as shown in (1.5),

$$\sigma = \frac{Nc}{\pi D} \quad (1.5)$$

where σ [-] is the solidity, N [-] is the number of blades, and c [m] is the chord length. Li, et al., [5] studied the relationship between the maximum power coefficient and solidity and resulted that the small solidity leads to increase TSR can provide the maximum power coefficient, and the power coefficient tends to decrease as solidity increases.

1.3.2 Aspect ratio

This thesis defines aspect ratio as shown (1.6),

$$AR = \frac{L}{c} \quad (1.6)$$

where $AR[-]$ is the aspect ratio of the blade. Naccache & Paraschivoiu [6] investigated the aspect ratio with the same solidity VAWTs and concluded that the large aspect ratio has a large power coefficient than that one. They compared the same solidity cases with different blade length used in VAWT, and discussed the for long blade one's power coefficient is closer to two-dimensional result.

1.4 Motivation of this thesis

To increase the power coefficient, the design space should be explored. In this work we explore this space with the help of CFD. Firstly, we recommend to focus only on three-dimensional CFD simulations. The drawback is that one simulation on a supercomputer takes more than two weeks to compute. Secondly, a variety of geometric features' results that some research groups investigated separately in each, should be compared. It leads to broad the range of comparison.

Three-dimensional simulations usually take a long-time computational time because the mesh need to be very fine in the boundary layer and the simulation is unsteady so a large number of rotations of the turbine need to be calculated. Even by using parallel processors on super computers computer, one full size wind turbine three-dimensional case required more than two weeks until to be converged. Furthermore, additional simulations may be needed for different revolution speeds to investigate different TSR. Before calculations, no one knows how many rpm is appropriate for the objective model. One model is usually simulated at least three or four revolutions to determine the ideal operation conditions. Therefore, one three-dimensional CFD cases take three or four months. Actually, some researchers published three-dimensional results, but the optimal operating condition has not been identified. It indicates one of the main drawbacks of CFD as being very expensive.

This thesis aims at finding relationships between geometric design parameters and performance based on large number of CFD simulations. The geometry of VAWTs has some decisive factors affecting the maximum power coefficient such as a rotor diameter, a blade length, a chord length, a wing thickness, a wing section, or supportive parts: shaft and arms. These elements can be combined into a projected area, a solidity, and aspect ratio. Solidity, especially, that is a rate of a rotation diameter with a chord length, is considered the most important factor for the maximum power coefficient. Some researchers concluded that the moderately small solidity VAWTs have a large maximum power coefficient in two-dimensional CFD. Of course, this topic has been studied, but it is still arguable based on three-dimensional simulation. Hence, this study assembles many case studies to compare some three-dimensional performance data and creates a certain model to predict the maximum power coefficients.

1.5 Overview of the Literature associated with CFD for VAWT

Early 2000, some CFD models were significantly developed alongside significant improvements of computer processing power. Furthermore, Mentor introduced DES k-omega SST to model turbulence, and some researchers applied started to simulate vertical axis wind turbines for performance evaluation using these models [7]. Actually, the number of papers of three-dimensional computational fluid dynamics cases began to increase gradually from that period and has reached more than a million cases. Especially DES k-omega SST is likely to match the CFD result to some experimental data. This option seems to be the most favorite for present day researchers but the simulations are mostly two dimensional CFD cases with fewer three-dimensional CFD cases. It is well documented that 2D simulations are much faster but less accurate than three-dimensional cases due to three-dimensional losses such as the tip-vortex.

The number of papers reporting three-dimensional CFD simulations of VAWT has been increasing for a decade and reached more than twenty per year on Google Scholar. The main reason is the improvement of cluster computing technologies. Usually, studies employ k-omega type of turbulence models in three-dimensional CFD. This type of turbulence model requires fine mesh and tiny time steps to calculate the power coefficient. Due to this, the number of three-dimensional cases is not large. Instead of that, a few cases are referred to the majority of studies. For example, the number of related papers is about 20 from about 1000 in 2019.

After 2010, the number of investigations for three-dimensional studies gradually increased as shown in Figure 3. These numbers are obtained by searching on Google scholar. The searching words are “VAWT or vertical axis wind turbine”, “3D or three dimension”, and “CFD or simulation”. Of course, all papers are not directly related to this study. Some papers are shown because they have the word of VAWT for author’s name, 3D, simulation. Also, there are some duplicated cases are published. In particular, the same large simulation can be discussed in many

papers with different points of view. Nevertheless, it is obvious that the number of papers in this area is significantly increasing.

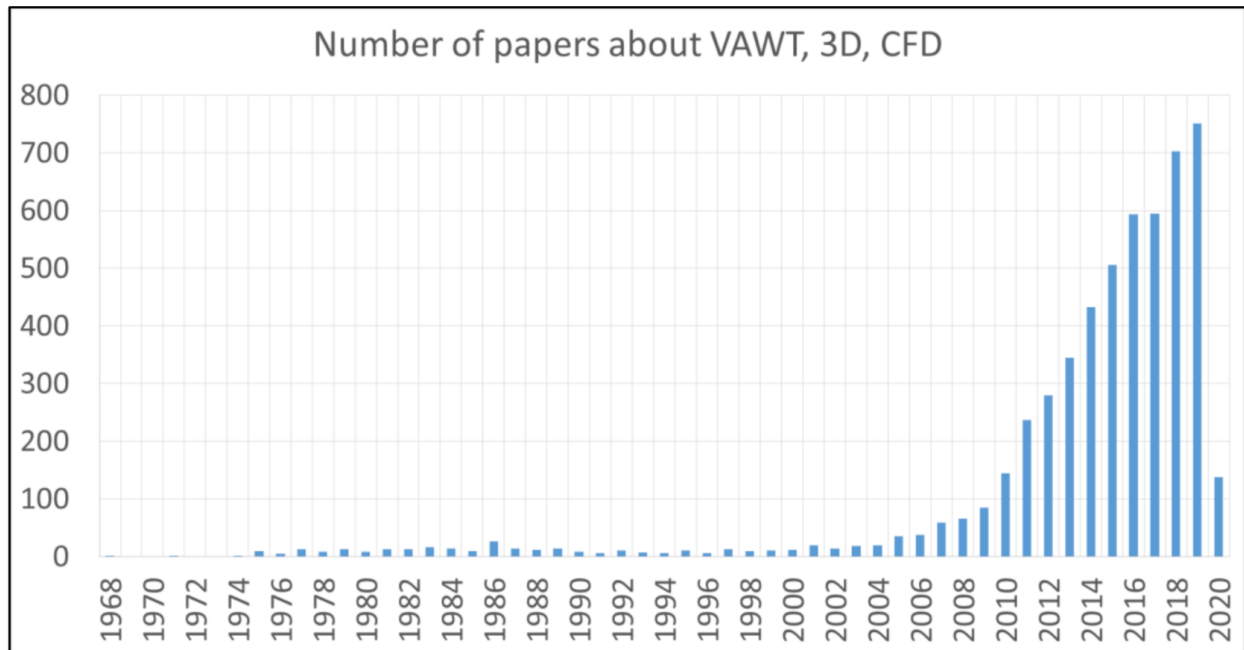


Figure 3 The number of papers about VAWT, 3D, CFD

Just a note on the Case study procedure used later to identify some relevant paper and associated turbines. The overall procedure is divided into five steps: gathering, screening, comparing, analyzing, and evaluating steps as shown in Figure 4. In gathering step, simply cases are gathered on Google scholar. As previously stated, adequate search words are used. The time period is from 2011 to 2020 April. This approach identified 28 cases to be used later.



Figure 4 Case study steps

1.6 Objectives

The overall goals of thesis are:

- Extract three-dimensional simulations results from the literature that can be used to study the effect of parameters on the performance of VAWTs;
- Simulate some of the three-dimensional CFD for VAWTs in the literature for consistency;
- Study the effect of some parameters on the power coefficient of VAWTs;
- Create simple models that can predict the power coefficient of VAWT without any large CFD simulations.

2 VAWT parametric study

In this Chapter, numerical simulation data available in the literature is analyzed to identify the main trends that affect the maximum power coefficient.

2.1 Maximum Power Coefficient (MaxCP) relationship to single key parameters

This section organizes the gathered dataset and illustrates how factors affect the maximum power coefficient. All reference cases are listed in Table 1. These cases reflect the highest Cp and the associated TSR for H type VAWT turbines. The calculations were all three-dimensional simulations of based on solving the Navier-Stokes equations. Different turbulence models were used. The following sub-sections discuss the relation of the Cp with key parameters.

Table 1 Cases

Case id	TSR	MaxCP	H	D	N	c	Wing section	Model	Ref
Case1	2.4	0.27	1.48	1.03	3	0.086	NACA0021	SST k- ω	[8]
Case2	1.53	0.26	3	2.5	3	0.4	NACA0015	SST k- ω	[9]
Case3	2.2	0.2	1.2	2	2	0.265	NACA0021	SST k- ω	[10]
Case4	2.4	0.27	1.48	1.03	3	0.086	NACA0021	SST k- ω	[11]
Case5	4.5	0.28	1	1	2	0.06	NACA0018	SST k- ω	[12]
Case6	2.25	0.17	1.2	2	2	0.265	NACA0021	IDDES SST k- ω	[13]
Case7	1.33	0.12	1.15	1.89	3	0.3	NACA0021	k- ϵ	[14]
Case8	2.3	0.18	1.2	2	2	0.265	NACA0021	IDDES SST k- ω	[15]
Case9	2.3	0.16	1.2	2	2	0.265	NACA0021	SST k- ω	[15]
Case10	3	0.26	0.5	0.75	2	0.08	NACA0018	SST k- ω	[16]
Case11	2.75	0.12	0.5	0.75	2	0.08	NACA0018	SST k- ω	[16]
Case12	1.5	0.28	3	2.5	3	0.4	NACA0015	SST k- ω	[17]
Case13	2.2	0.325	7.2	3	3	0.442	NACA0020	SST k- ω	[18]
Case15	2.70	0.25	2.91	1.03	3	0.086	NACA0021	SST k- ω	[19]
Case16	6.9	0.2	2	2.5	3	0.2	NACA0015	RNG k- ϵ	[20]
Case17	2.2	0.373	3	2.7	2	0.42	NACA0015	Transition SST	[21]
Case18	2	0.334	3	2.7	3	0.42	NACA0015	Transition SST	[21]
Case19	1.25	0.21	0.8	0.8	3	0.2	NACA0021	LES	[22]
Case20	1.8	0.22	0.4	0.6	2	0.1	NACA0022	RNG k- ϵ	[23]
Case21	2.2	0.182	2	4	3	0.4	NACA0015	RNG k- ϵ	[24]
Case22	2.2	0.2	1.2	2	2	0.265	NACA0021	IDDES SST k- ω	[25]
Case23	1.6	0.33	3	2.5	3	0.4	NACA0015	SST k- ω	[26]
Case24	1.3	0.19	0.8	0.8	3	0.2	NACA0018	SST k- ω	[27]
Case25	2.24	0.27	0.81	0.6	3	0.081	NACA0018	SST k- ω	[28]
Case26	5	0.23	3	2	3	0.2	NACA0015	LES	[29]
Case27	2.5	0.34	1	1	2	0.12	NACA0018	Realizable k- ϵ	[30]
Case28	2.6	0.325	1.43	0.515	3	0.15	NACA0018	Realizable k- ϵ	[31]

2.1.1 Maximum power coefficient vs Solidity

As discussed in previous sections, solidity is considered to affect the maximum power coefficient. For example, A. Subramanian et al., concluded that the maximum power coefficient increases as solidity increases in the lower TSR region [34]. Nevertheless, by presenting the maximum C_p versus solidity for all 28 cases in Figure 5, it is not possible to identify any specific behavior. The maximum power coefficient fluctuates without any relationship to the solidity. For low solidity, we have a range of maximum C_p from 0.1 to 0.36.

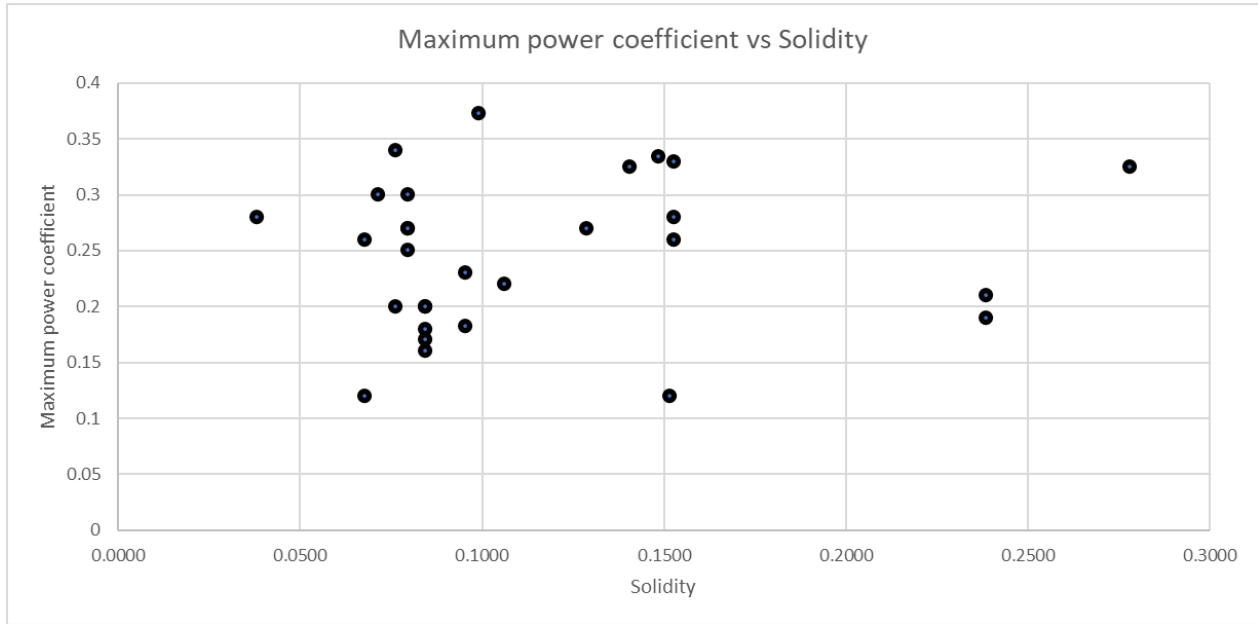


Figure 5 Maximum power coefficient vs Solidity

To further analyse if solidity is a dominant factor, cases that have no shaft or arms, are compared shown in Figure 6 and 7. The supportive part or the turbulence model seem not to affect to the maximum power coefficient. The maximum power coefficient is different with the same solidity geometry.

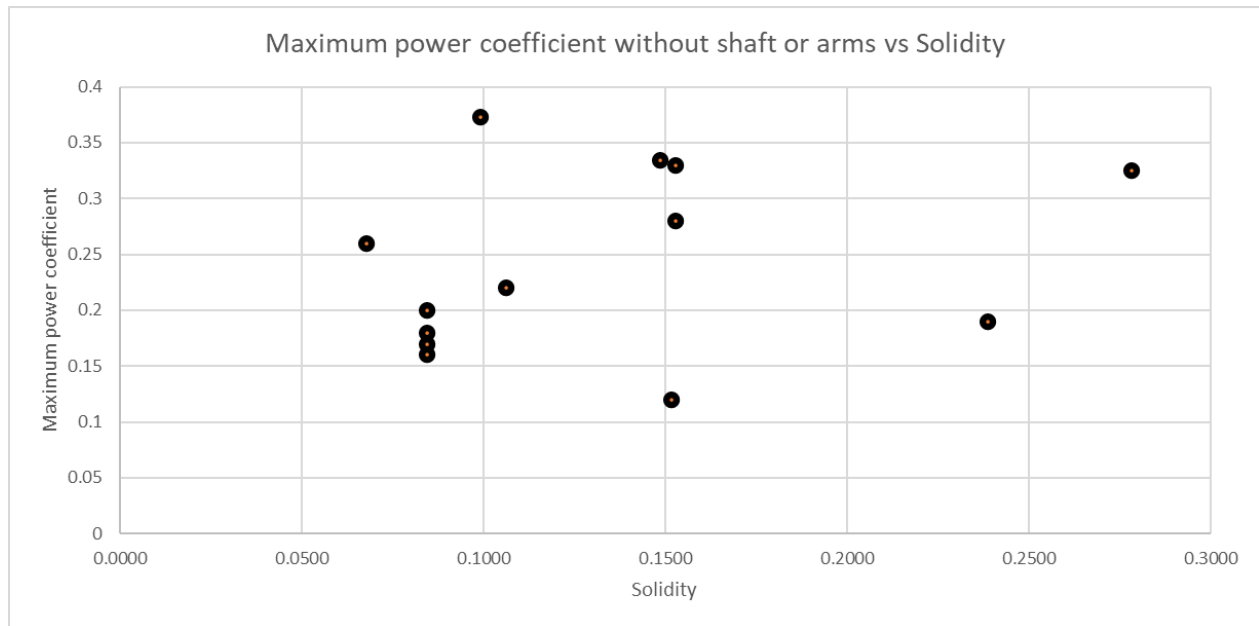


Figure 6 Maximum power coefficient without shaft or arms vs Solidity

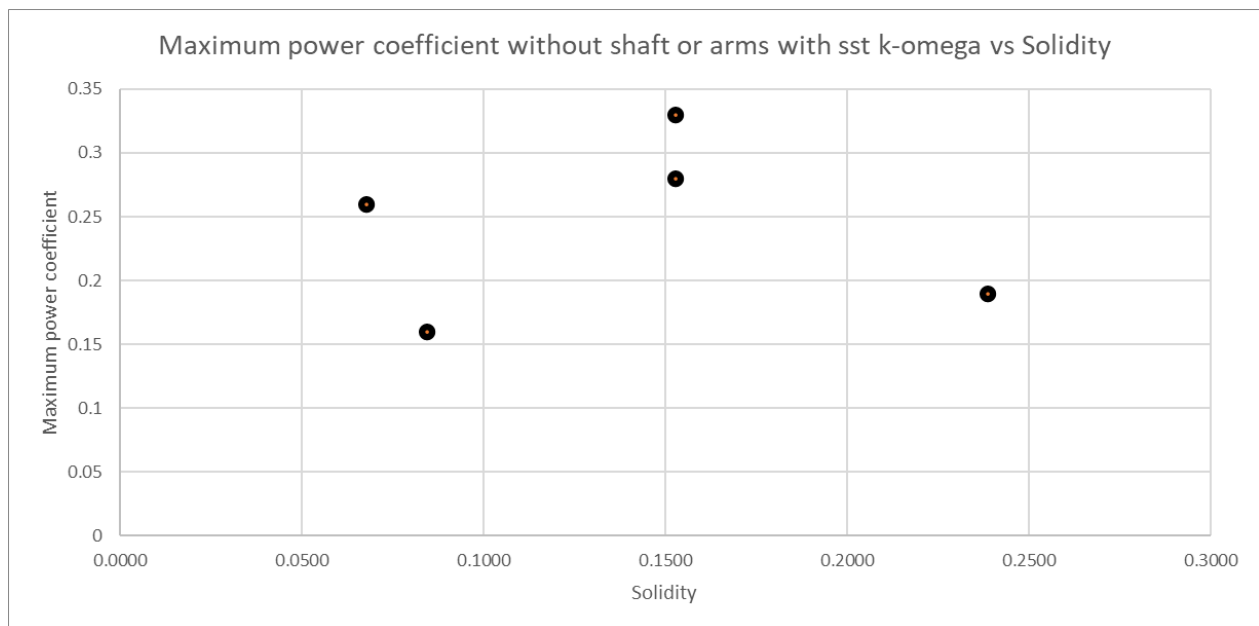


Figure 7 Maximum power coefficient without shaft or arms with sst k-omega vs Solidity

2.1.2 TSR for the maximum power coefficient vs Solidity

The higher solidity roughly shows in Figure 9 that the TSR for the maximum power coefficient is lower and is higher for lower solidity. As Subramanian et al., discussed, solidity affect TSR for the maximum power coefficient [34].

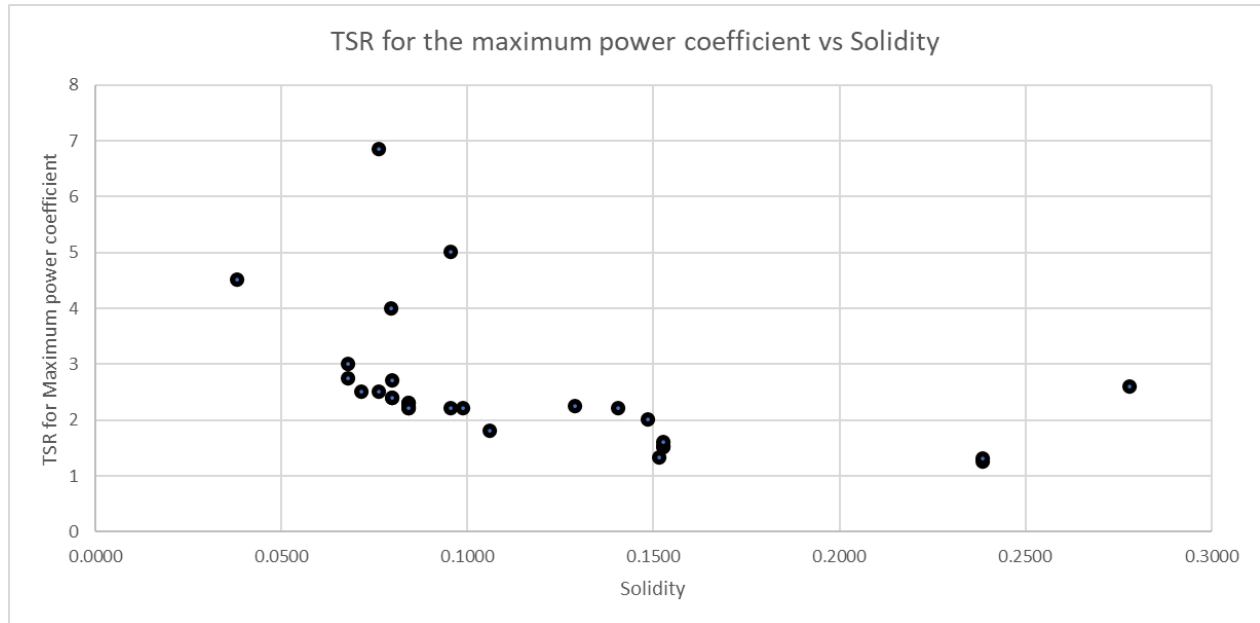


Figure 8 TSR for the maximum power coefficient vs Solidity

2.1.3 Maximum power coefficient vs number of blades

Compared with different number of blades cases, there is no relationship between the maximum power coefficient and the number of blades as shown Figure 10. The effect of the number of blades is often discussed in the literature but does not appear to be very relevant.

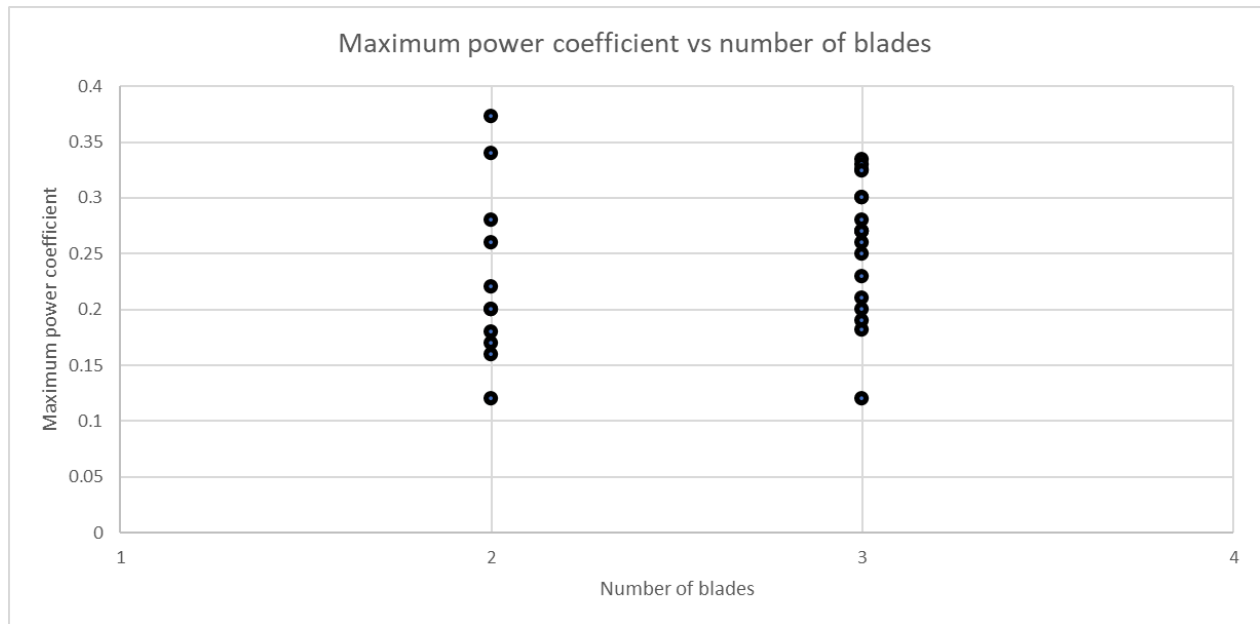


Figure 9 Maximum power coefficient vs number of blades

As shown in Table 2, we compare maximum power coefficients with almost the same solidity cases for different number of blades. It is still difficult to find any relationships between maximum power coefficient and number of blades.

Table 2 Comparison for the number of blades with almost the same solidity cases

Case ID	Solidity	Max Cp	N
11	0.0679	0.12	2
14	0.0716	0.3	3
27	0.0764	0.34	2
16	0.0764	0.2	3
4	0.0797	0.27	3
3	0.0844	0.2	2
22	0.0844	0.2	2
21	0.0955	0.182	3
26	0.0955	0.23	3
17	0.0990	0.373	2
20	0.1061	0.22	2
25	0.1289	0.27	3

2.1.4 Maximum power coefficient vs aspect ratio

As Naccache & Paraschivoiu [6] studied, higher aspect ratio approaches the Betz-Joukowsky limit. Note that a small aspect ratio leads a small maximum CP.

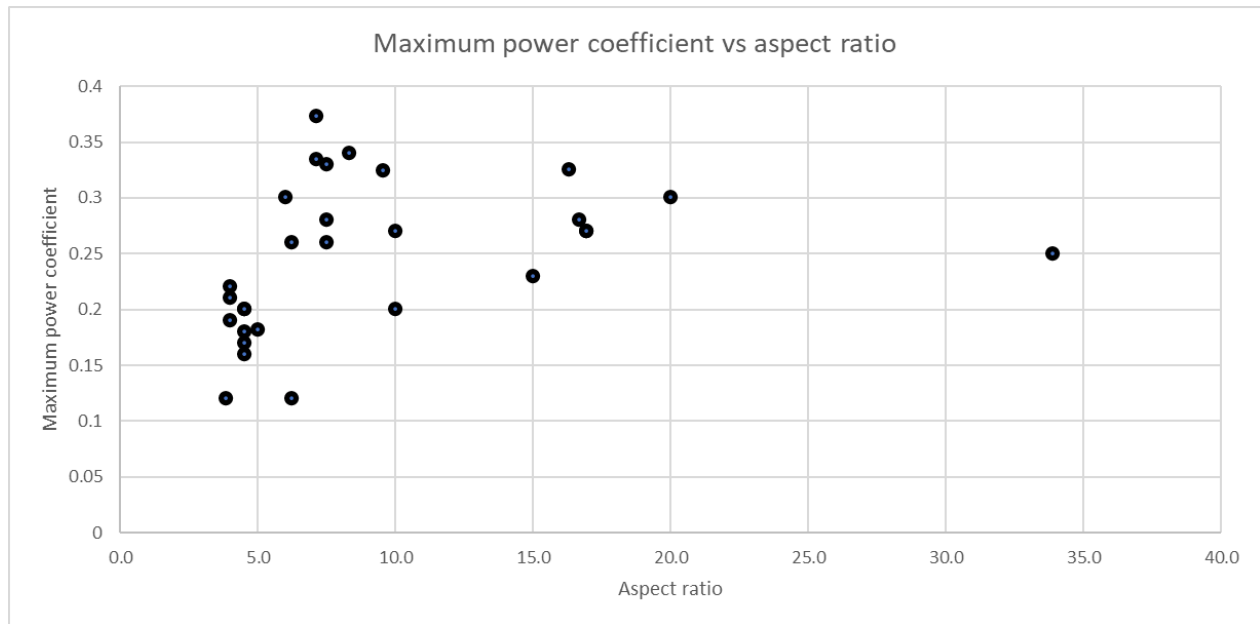


Figure 10 Maximum power coefficient vs aspect ratio

Increasing the aspect ratio leads to the higher maximum power coefficient due to the three-dimensional effect, in particular the tip effect which is less important as the blade is longer for the same chord. Increasing aspect ratio leads to long spanwise blades. The three-dimensional losses such as tip vortex generate induced drag on the VAWT. Two-dimensional cases have higher power coefficient than three-dimensional cases [6].

This trend clearly shows for cases that have no shaft and no arms as shown in Figure 11 although the number of cases is few.

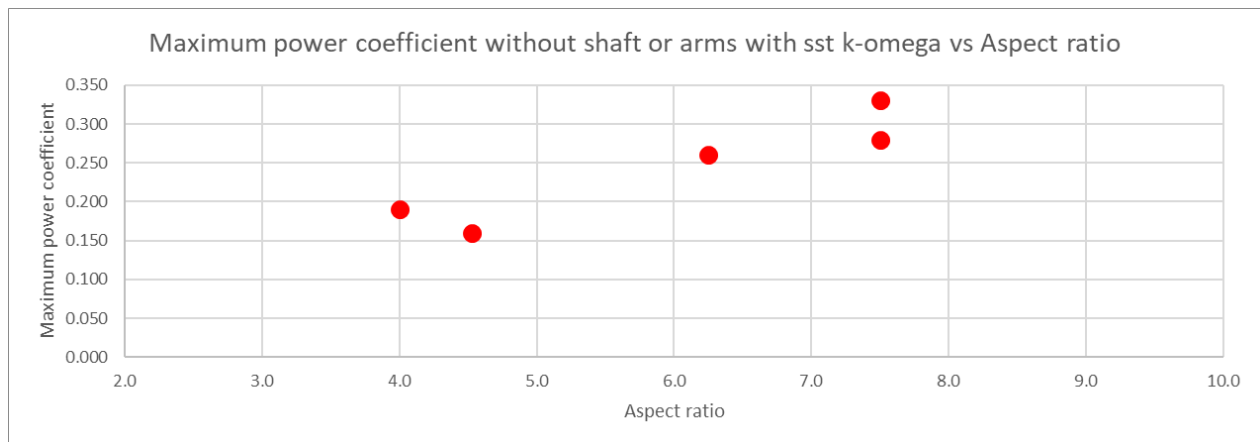


Figure 11 Maximum power coefficient without shaft or arms with sst k-omega vs Aspect ratio

2.1.5 Maximum power coefficient vs ratio of wing thickness to chord

This subsection compares cases for different ratios of wing thickness to chord as shown in Figure 12. It clearly shows that maximum power coefficient increases as the blade thickness decreases. This trend is emphasized focusing on the maximum power coefficient without shaft or arms with the *SST k - ω* turbulence model as shown in Figure 13.

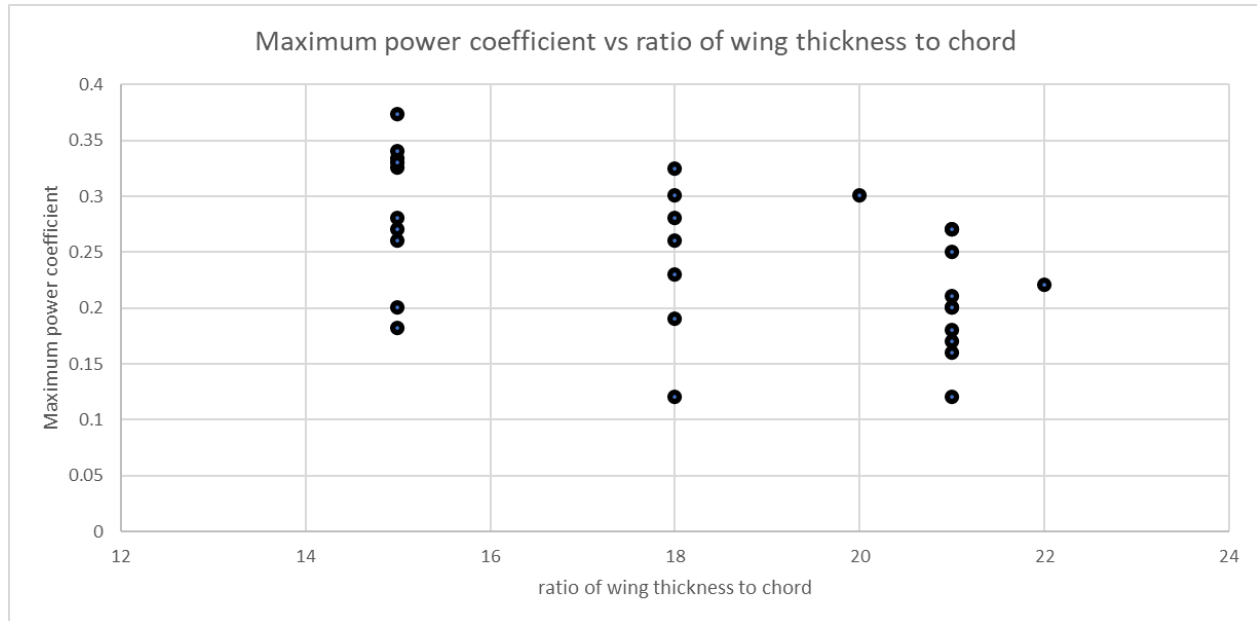


Figure 12 Maximum power coefficient vs ratio of wing thickness to chord

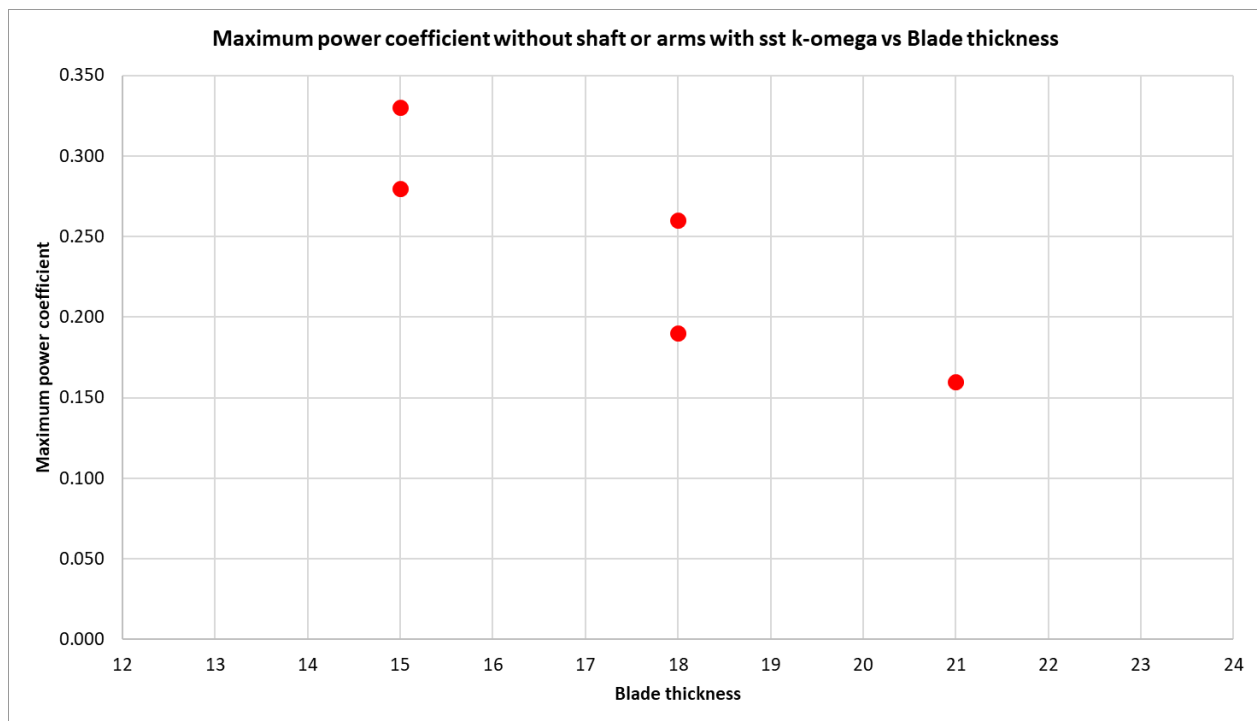


Figure 13 Maximum power coefficient without shaft or arms with sst k-omega turbulence model

2.1.6 Maximum power coefficient vs projected area

Maximum power coefficient increases as projected area increases as shown in Figure 1. The area of case 17, 18, 28 and 13 exceed $8.1 \text{ [m}^2\text{]}$, and their power coefficients are more than 0.3 [-] . On the other hand, the cases that have less than $0.64 \text{ [m}^2\text{]}$ of projected area have less than 0.3 [-] of power coefficient.

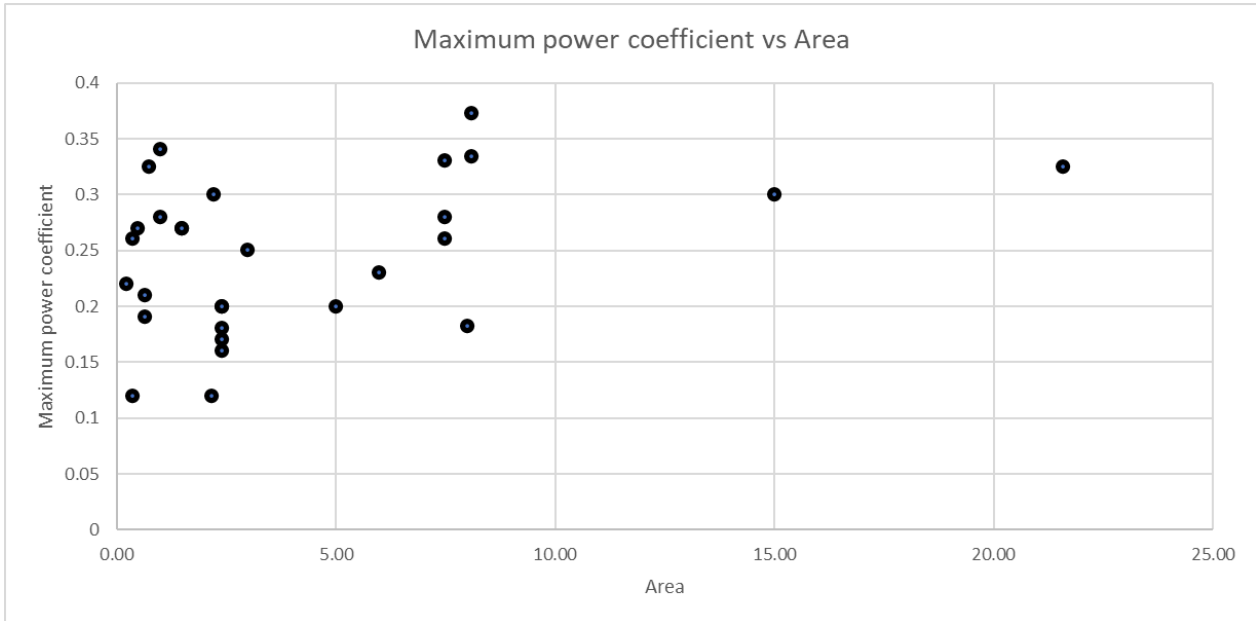


Figure 14 Maximum power coefficient vs Area

Also, the cases without shaft or arms with the *SST* $k - \omega$ model show the same trend as shown in Figure 15 although the number of cases is very few.

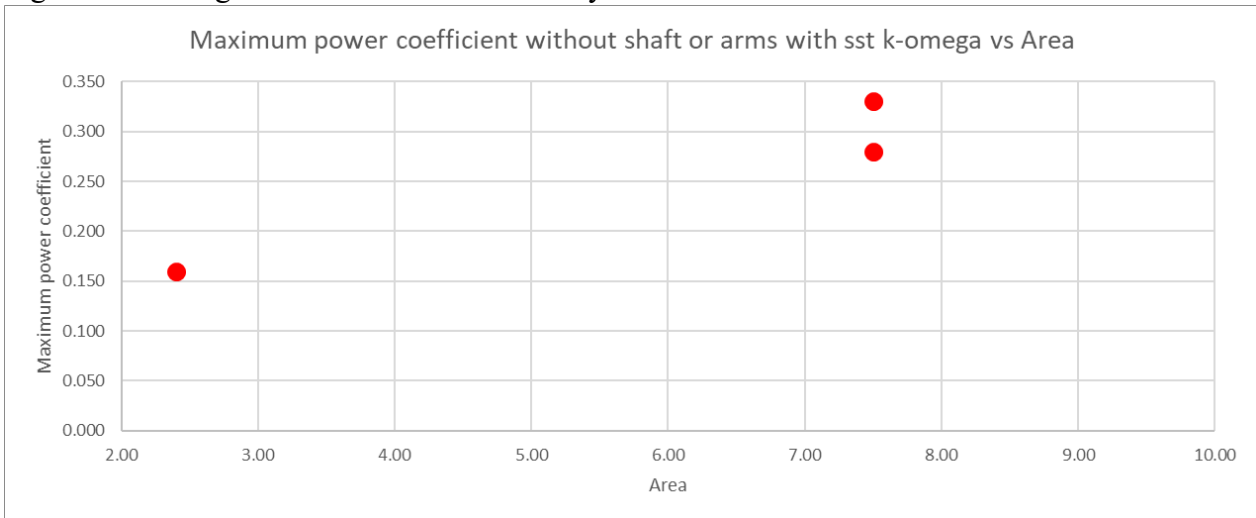


Figure 15 Maximum power coefficient without shaft or arms with sst k-omega vs Area

2.1.7 Difference of turbulence model

Some cases that employ the same turbulence model show some trends. First, IDDES $SST k - \omega$ cases have relatively small power coefficient. Case 6, 8, and 22 apply IDDES $SST k - \omega$ and their power coefficients are less than 0.2. Second, cases that apply RNG $k - \epsilon$ also have small power coefficients. Case 16, 20, and 21 use RNG $k - \epsilon$ and their power coefficients are less than 0.22. LES (Large Eddy Simulation) cases accordingly show small power coefficient. On the other hand, cases that use Realizable $k - \epsilon$ or Transition SST have relatively higher power coefficient. As for the cases based on $SST k - \omega$ have a variation of power coefficient. It is from 0.12 to 0.33. Note that the preferred model today is the $SST k - \omega$ turbulence model.

Table 3 C_p for different turbulence models

Case	Max power coefficient	Model
6	0.17	IDDES SST k-omega
8	0.18	IDDES SST k-omega
22	0.2	IDDES SST k-omega
20	0.22	RNG k-epsilon
16	0.2	RNG k-epsilon
21	0.182	RNG k-epsilon
17	0.373	Transition SST
18	0.334	Transition SST
19	0.21	LES
26	0.23	LES

2.1.8 Coefficient of determination between MaxCP and parameters

This subsection provides the coefficient of determination, addressed as R^2 , between MaxCP and parameters as shown in Table 4. These cases focus only no shaft and no arms geometries. This shows what parameters can determine MaxCP for the VAWT. R^2 is the non-dimensional value between -1 to 1, that indicates correlation. Usually, it has an intense correlation if it is from 0.6 to 0.8. Having about 0.5 shows the medium correlation. If it has from 0.2 to 0.4 the correlation is weak, and the less of 0.2 means few relationships.

Table 4 Coefficient of determination between MaxCP and parameters

Parameter	R^2
Blade thickness	0.682173
Aspect ratio	0.737244
Solidity	0.125036

2.1.9 Summary of the analysis between MaxCP and single parameters

The analysis between MaxCP and single parameters shows some findings as follows:

- Higher aspect ratio may increase the maximum power coefficient.
- Higher projected area may increase the maximum power coefficient, but the coefficient of determination is low.
- Lower blade thickness may increase the maximum power coefficient
- The other parameters that include solidity show an unclear relationship to the maximum power coefficient.

2.2 Maximum Power Coefficient (MaxCP) relationship to combinations of factors

This section compares power coefficients with a combination of factors. As discussed previously, some factors clearly affect the maximum power coefficient. The question in this section is to explore if a combination of factors can be identified. So, the following subsections try to highlight which parameters can be interacting.

2.2.1 Combination of solidity and area

This subsection focuses on the combination of solidity and aspect ratio. Figure 17 shows the relationship between both solidity and aspect ratio with their power coefficients. The red triangular case has the smallest power coefficient from 0 to 0.2. The blue diamond has the high-power coefficient that is over 0.3. The series of power coefficient from 0.2 to 0.3 is removed.

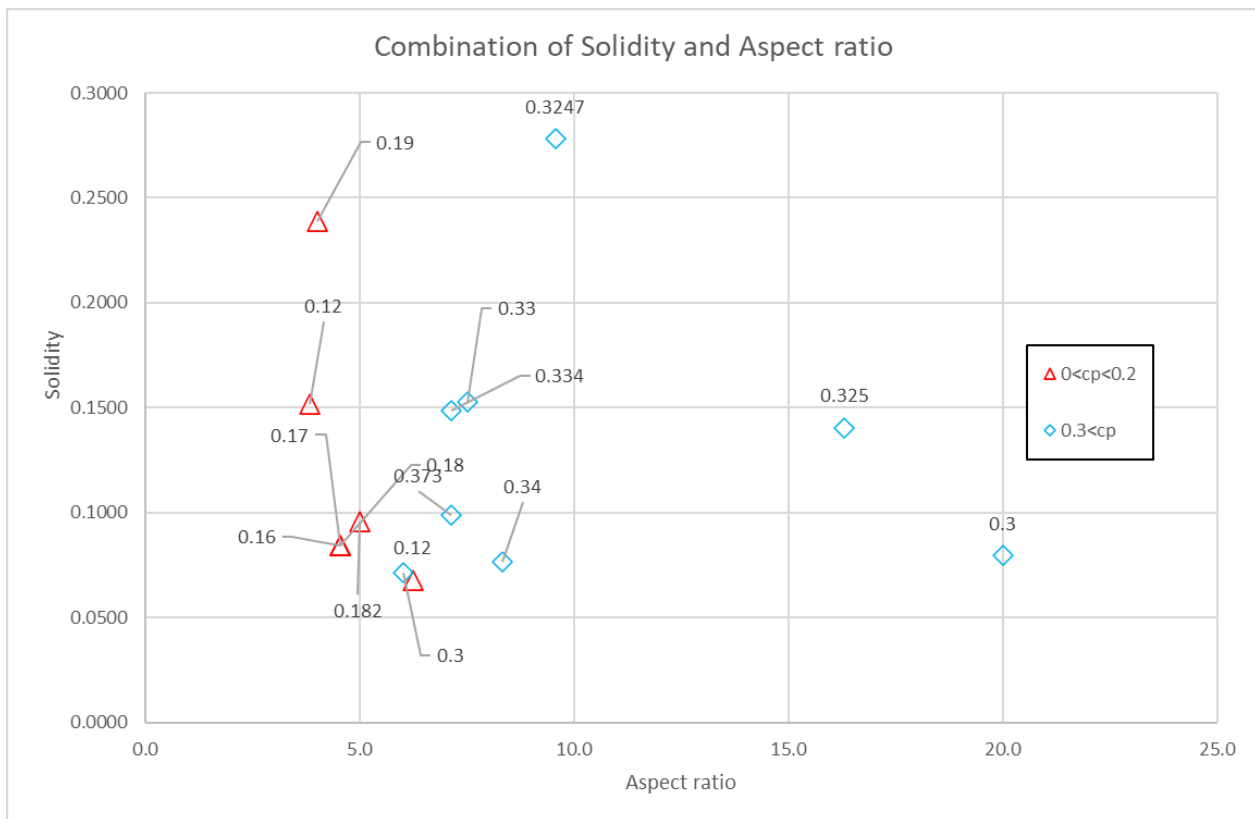


Figure 16 Combination of Solidity and Aspect ratio

Although an aspect ratio of red triangle case is located to the right side of blue cases', the high aspect ratio cases have roughly higher power coefficient. On the other hand, solidity doesn't seem to show any contributions for power coefficient.

2.2.2 Combination of Area and Solidity

This subsection focuses on the combination of area and solidity. Figure 18 shows the relationship between these parameters. This picture indicates that the lower power coefficient case has the lower projected area. However, some cases correspond to their area and solidity with the different power coefficient.

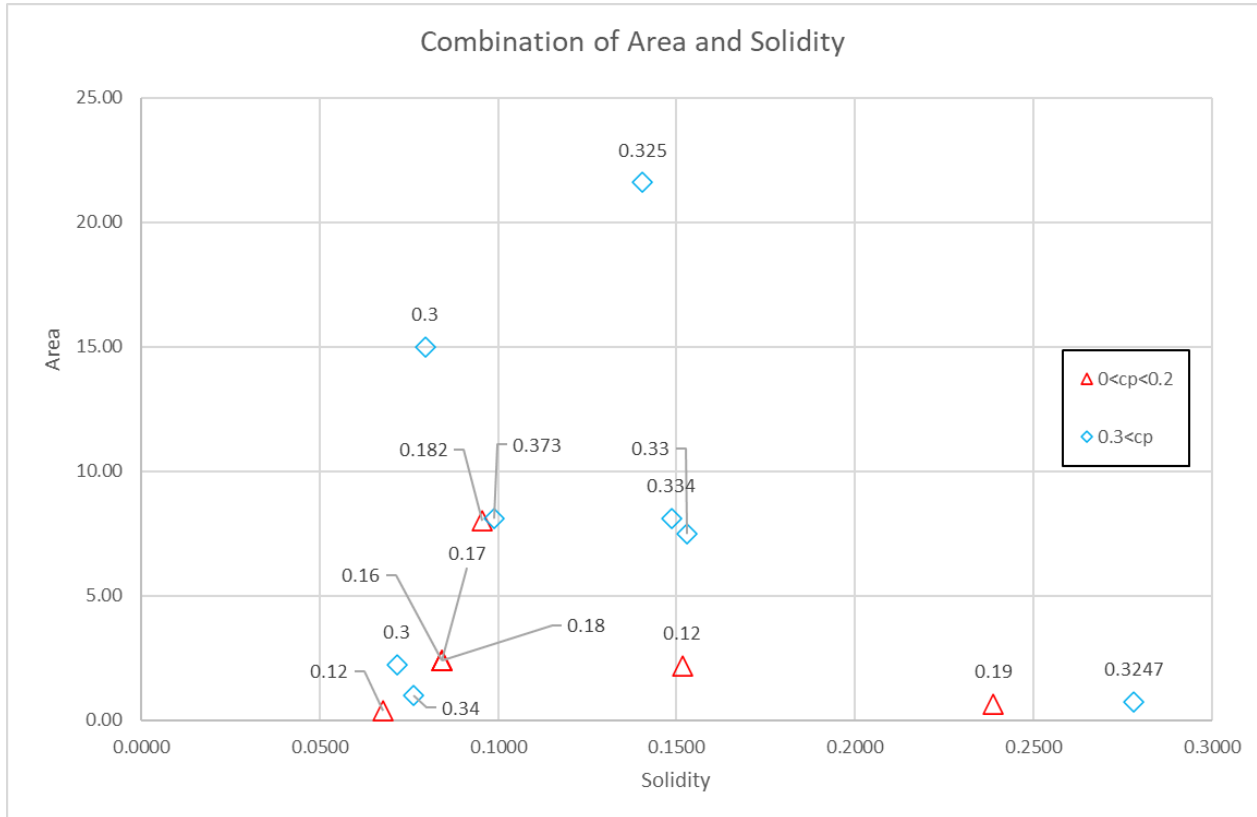


Figure 17 Combination of area and solidity

2.2.3 Combination of area and aspect ratio

The combination of area and aspect ratio is shown in Figure 19. This graph also shows that the higher aspect ratio leads to the higher power coefficient. Blue diamond cases are located in the right upper side of the picture, and the red triangular cases are close to the origin of the graph. This indicates that large turbines with large area and high blade aspect ratio perform better.

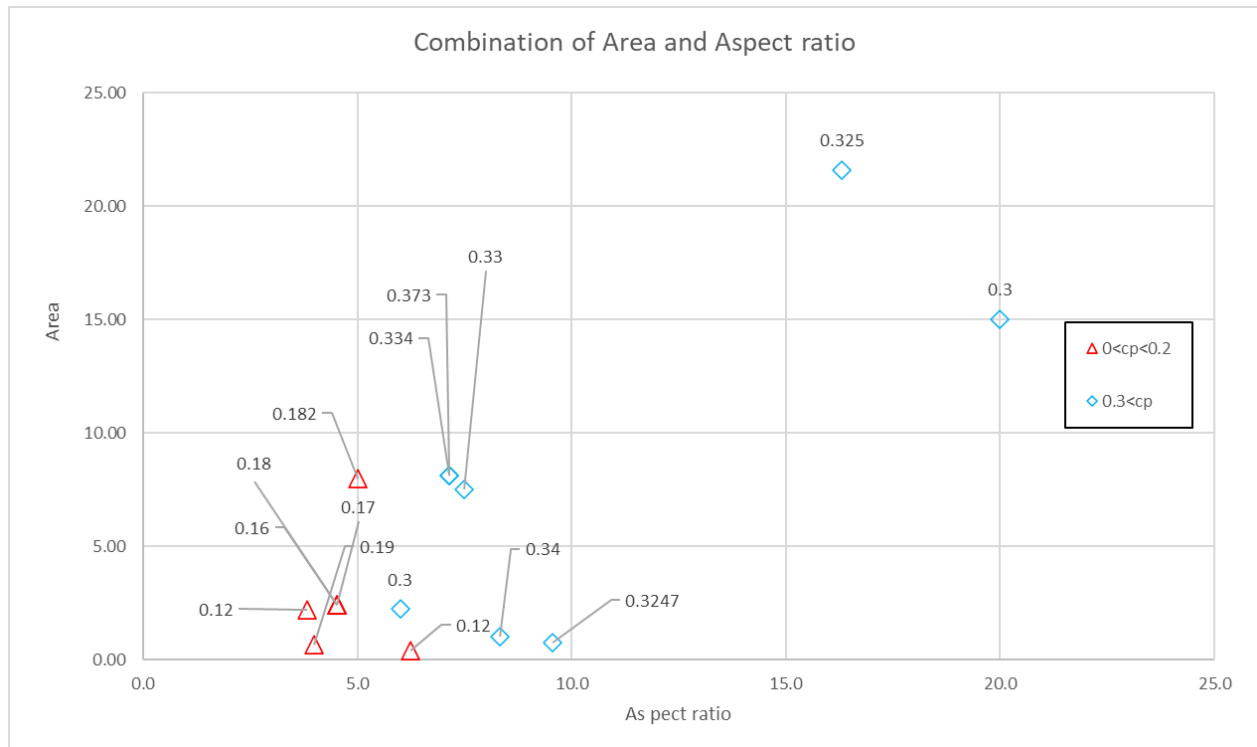


Figure 18 Combination of area and aspect ratio

2.2.4 Combination of blade thickness and aspect ratio

The combination of blade thickness and aspect ratio is shown in Figure 19. It is clearly that red triangles are located in the left side of the scatter plot. As for blue diamonds, it is located in the lower of the plot. When removing the effect of supportive parts, Figure 20 focuses on only turbine data with no shaft and no arms cases. This picture clearly shows the trend that the small blade thickness and large aspect ratio lead to large power coefficient. In detail, larger than 6.0 aspect ratio and smaller than 18% of the thickness ratio to the chord length cases have more than a large power coefficient, 0.26.

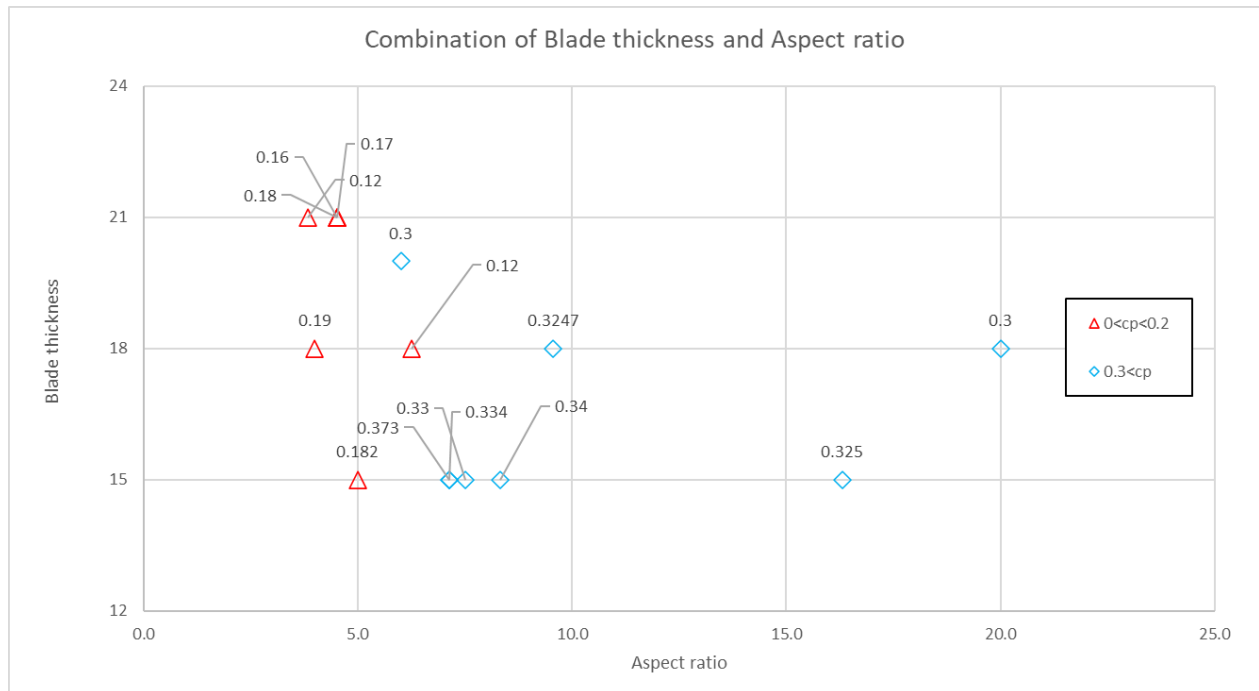


Figure 19 Combination of blade thickness and aspect ratio

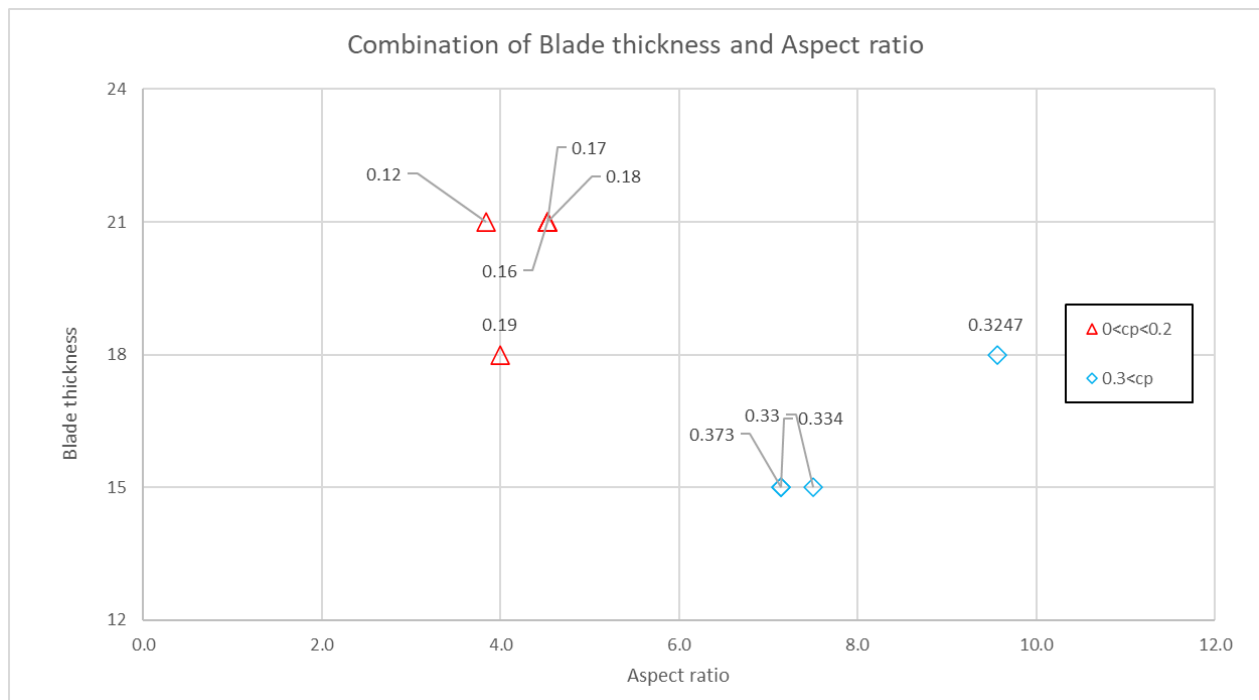


Figure 20 Combination of blade thickness and Aspect ratio without shaft and arms

2.2.5 Summary of the analysis between MaxCP and combinations of parameters

The analysis between MaxCP and multiple parameters shows some findings as follows:

- The higher aspect ratio and the smaller blade thickness can lead to the higher power coefficient;
- Large turbine which typically have large areas and large aspect ratios perform better;
- The solidity and projected area do not seem to affect to the power coefficient.
- Trends clearly appear, but it is difficult to determine the function that can calculate MaxCP directly due to the small number of cases.

The following chapter complements some cases with no shaft no arms, in order to create some model functions to describe the power coefficient without large simulations.

3 CFD simulations

In this Chapter, the methodology to simulate the flow around VAWTs is presented. The motivation is based on running additional cases to calculate the C_p for some cases found in the literature but the geometry will be changed to remove the shaft and arms. These cases will be added to the pool to increase the number of data points.

3.1 Govern equations and simulation software

CFD is employed by using STAR-CCM+ by Siemens Digital Industries Software. This commercial solver applied the finite volume method for CFD, and a methodology is developed to apply it to the VAWT.

This CFD software computes the fundamental laws that are conservation of mass, conservation of momentum, and conservation of energy as follows,

$$\frac{\partial \rho}{\partial t} + \nabla \cdot (\rho \vec{u}) = 0 \quad (3.1)$$

where \vec{u} is the continuum velocity. The time rate of change of linear momentum is equal to the resultant force acting on the continuum:

$$\frac{\partial(\rho \vec{u})}{\partial t} + \nabla \cdot (\rho \vec{u} \otimes \vec{u}) = \nabla \cdot \vec{\sigma} + \vec{f}_b \quad (3.2)$$

where \otimes denotes the Kronecker product, \vec{f}_b is the resultant of the body forces, and $\vec{\sigma}$ is the stress tensor.

$$\frac{\partial(\rho E)}{\partial t} + \nabla \cdot (\rho E \vec{u}) = \vec{f}_b \cdot \vec{u} + \nabla \cdot (\vec{u} \cdot \vec{\sigma}) - \nabla \cdot \vec{q} + S_E \quad (3.3)$$

where E is the total energy per unit mass, \vec{q} is the heat flux, and S_E is an energy source per unit volume.

This applied constant density as follows.

$$\rho = \rho_0 \quad (3.4)$$

where ρ_0 is a constant. [35]

3.2 Segregated Flow Solver

The segregated flow solver solves the integral conservation equations of mass and momentum in a sequential manner. The non-linear governing equations are solved iteratively one after the other for the solution variables. The segregated solver employs a pressure-velocity coupling algorithm where the mass conservation constraint on the velocity field is fulfilled by solving a pressure-correction equation. The pressure-correction equation is constructed from the continuity equation and the momentum equations such that a predicted velocity field is sought that fulfills the

continuity equation, which is achieved by correcting the pressure. This thesis applied a pressure-velocity coupling algorithms, SIMPLE method. [35]

3.2.1 SIMPLE method

SIMPLE (Semi-implicit method for pressure-linked equation) method is employed for the pressure-velocity coupling algorithm in STAR-CCM+. This method computes provisory information and is corrected by the discretized momentum equation. Subsequently, it updates the pressure corrections and corrects the face mass fluxes and cell velocities. This method is widely used in VAWT simulation and is suggested that it is advantageous to employ to the VAWT simulation. [36]

3.2.2 RANS

This chapter introduces the turbulence model that this work employed. CFD simulation usually employs turbulence model to decrease a huge computational cost compared with the DNS (Direct numerical simulation). The turbulence models are simply divided into three as shown in Figure 21.

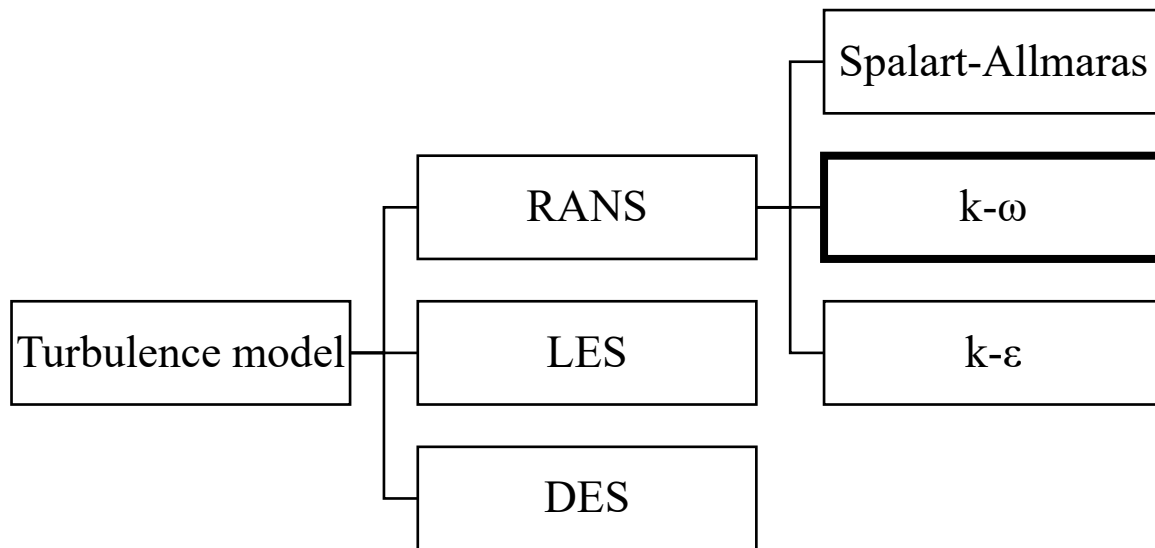


Figure 21 Type of turbulence model

This thesis solves RANS (Reynolds-Averaged Navier-Stokes) equations. This provides closure relations for the Reynolds-Averaged Navier-Stokes equations, that govern the transport of the mean flow quantities. To obtain the Reynolds-Averaged Navier-Stokes equations, each solution

variable ϕ in the instantaneous Navier-Stokes equations is decomposed into its mean, or averaged, value $\bar{\phi}$ and its fluctuating component ϕ' .

$$\phi = \bar{\phi} + \phi' \quad (3.5)$$

where ϕ represents velocity components, pressure, energy, or species concentration.

The averaging process may be thought of as time-averaging for steady-state situations and ensemble averaging for repeatable transient situations. Inserting the decomposed solution variables into the Navier-Stokes equations results in equations for the mean quantities.

3.2.3 SST $k - \omega$

SST $k - \omega$ computes the eddy viscosity in the Reynolds-Averaged Navier-Stokes equations. Mentor modified $k - \omega$ model that was proposed by Wilcox [7] [37]. The turbulent eddy viscosity μ_t is calculated as:

$$\mu_t = \rho k T \quad (3.6)$$

T is the turbulent time scale. The turbulent time scale is calculated using Durbin's realizability constraint as [38]:

$$\min\left(\frac{\alpha^*}{\omega}, \frac{\alpha_1}{SF_2}\right)$$

where α^* is a model coefficient, S is defined as the mean strain rate. The mean strain rate is defined as:

$$S = \sqrt{2\vec{S}:\vec{S}^T} \quad (3.7)$$

$$\vec{S} = \frac{1}{2}(\nabla\vec{u} + \nabla\vec{u}^T) \quad (3.8)$$

F_2 is a blending function calculated as:

$$F_2 = \tanh\left(\left(\max\left(\frac{2\sqrt{k}}{\beta^*\omega d}, \frac{500\nu}{d^2\omega}\right)\right)^2\right)$$

where β^* is a model coefficient, d is the distance to the wall.

The transport equations for the kinetic energy k and the specific dissipation rate ω are:

$$\frac{\partial}{\partial t}(\rho k) + \nabla(\rho k\vec{u}) = \nabla[(\mu + \sigma_k\mu_t)\nabla k] + P_k - \rho\beta^*f_{\beta^*}(\omega k - \omega_0 k_0) + S_k \quad (3.9)$$

$$\frac{\partial}{\partial t}(\rho\omega) + \nabla(\rho\omega\vec{u}) = \nabla[(\mu + \sigma_\omega\mu_t)\nabla\omega] + P_\omega - \rho\beta f_\beta(\omega^2 - \omega_0^2) + S_\omega \quad (3.10)$$

where μ is the dynamic viscosity, σ_k and σ_ω are model coefficients.

P_k and P_ω are production terms that are defined as (3.11)(3.12):

$$P_k = G_k + G_{nl} + G_b \quad (3.11)$$

$$P_\omega = G_\omega + D_\omega \quad (3.12)$$

where G_k is the turbulent production, G_{nl} is the non-linear production, G_b is the buoyancy production, G_ω is the specific dissipation production, and D_ω is the cross-diffusion term, respectively. Their definition is based on the user guide of STAR-CCM+ [35].

3.2.4 Implicit method setup

This thesis applied an implicit solver. The advantage of implicit solver is the higher CFL (Courant-Friedrichs-Lewy) condition number. This thesis divides one revolution into 720, 0.5 degrees, for each time step in common case. Moreover, the time discretization is 2nd order.

3.3 Geometry overview

This section provides how the control volume is meshed. First, the geometry parameters are defined for both the computational domain and the rotational domain where the turbine rotor is placed. Second, the boundary conditions are defined. Third, the geometric parameters of different turbine cases of interest are listed.

3.3.1 Geometry

The model is divided into two parts: a rotational part and a stationary part as shown in Figure 22. The shaded area indicates the rotational cylindrical area. This example has three blades in the rotational domain. The transparent cubic part is along with the original three-dimensional coordinates. Usually, the uniform flow spreads as the flow goes through the wind turbine. In this thesis, x-direction is the uniform free stream direction. The z-direction indicates the three-dimensional thickness. This work models two or three blades type of VAWTs and are placed in the rotational region. This domain is located in the frontal side with respect to the inlet of uniform flow of the entire computational domain. The rotational region is connected to the bottom surface of the cubic region. The bottom surface is a symmetrical plane, so that the actual negative z-direction has the opposite side of blades. Both bottom planes are aligned to the same z positions.

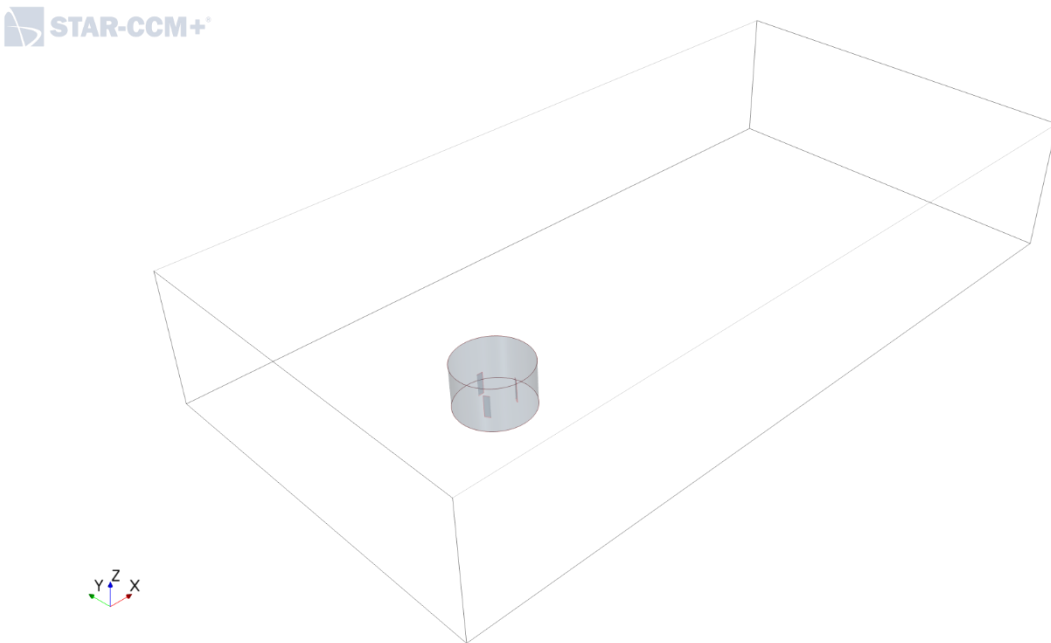


Figure 22 Computational domain and rotational region

The rotational region diameter is the double of the rotor diameter as shown in Figure 23. The outer circle indicates the surface of the rotational region, and the inner dashed line indicates the rotational diameter. Blades volume is treated as an empty space. Along with this, the surface layers wrap around blades volume. The layer is implemented by prism layer on STAR-CCM+. This option can handle the number of layers, the shape of cells, and how to growth from the wall boundary. Lastly, the buffer area slightly connects from the layer to the outer stationary region. Note that the gap between two regions should be small. In this work it is limited to about 20% from the small cell.

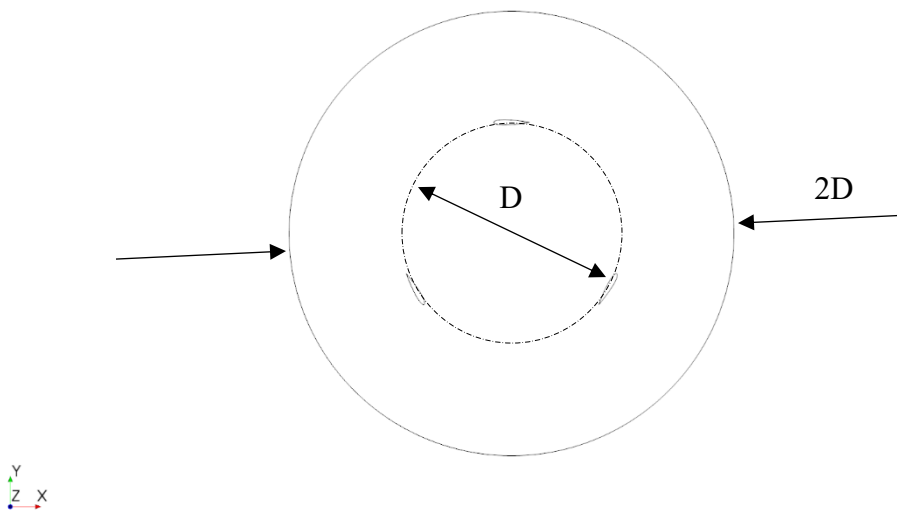


Figure 23 Rotational domain top view

As for the region between the end of the blades and the top of the rotation region, it is the same size as the blade length as shown in Figure 24. The dark shaded region is the blade region. The height of the rotational region is the double of the blade length.

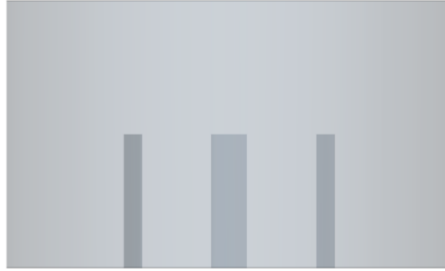


Figure 24 Rotational domain side view

3.3.2 Boundary conditions

The proposed model applies symmetrical condition to the central plane of VAWT to decrease the total amount of elements as shown in Figure 25. The symmetrical planes are set to the both rotational and stationary parts at z position equal to zero. This method is applied to a lot of cases, and Franchina et al. have validated this approach. [8]

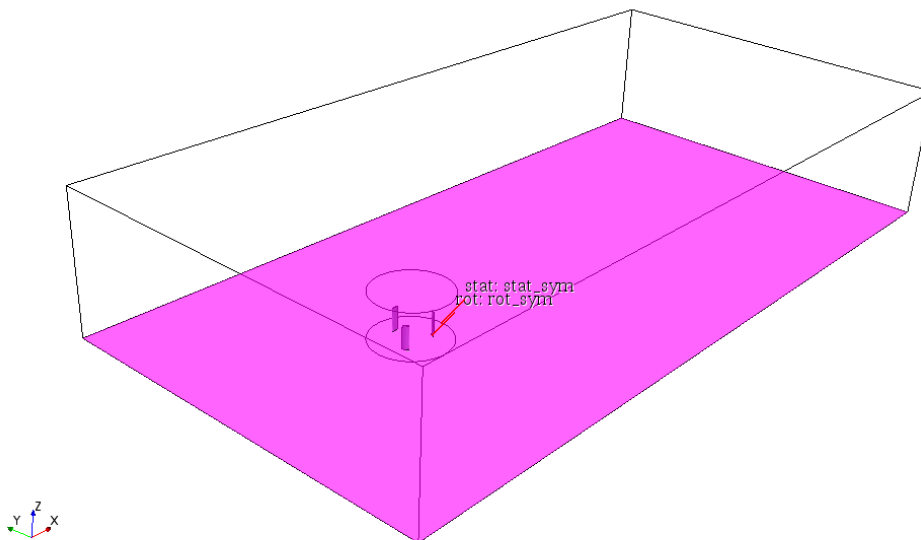


Figure 25 Symmetrical plane

There are two faces in the longitudinal directions on the cubic control volume. Those faces are the inlet and the outlet boundary conditions. The inlet boundary condition is located to the direction that is close to the rotational region. This research applied the uniform fixed velocity inlet boundary condition to the inlet. Some specified values are Table 5.

Table 5 Inlet boundary condition

Item	Value	Unit
Velocity	5.0	m/s
Turbulence Intensity	0.01	-
Turbulence Viscosity Ratio	10.0	-
Flow direction	Normal to the surface	-

The other side sets the outlet boundary condition. This condition is pressure outlet boundary condition, and it is specified in Table 6.

Table 6 Outlet boundary condition

Item	Value	Unit
Pressure	101325.0	kg m/s ²
Turbulence Intensity	0.01	-
Turbulence Viscosity Ratio	10.0	-

The relation between two conditions are shown in Figure 26.

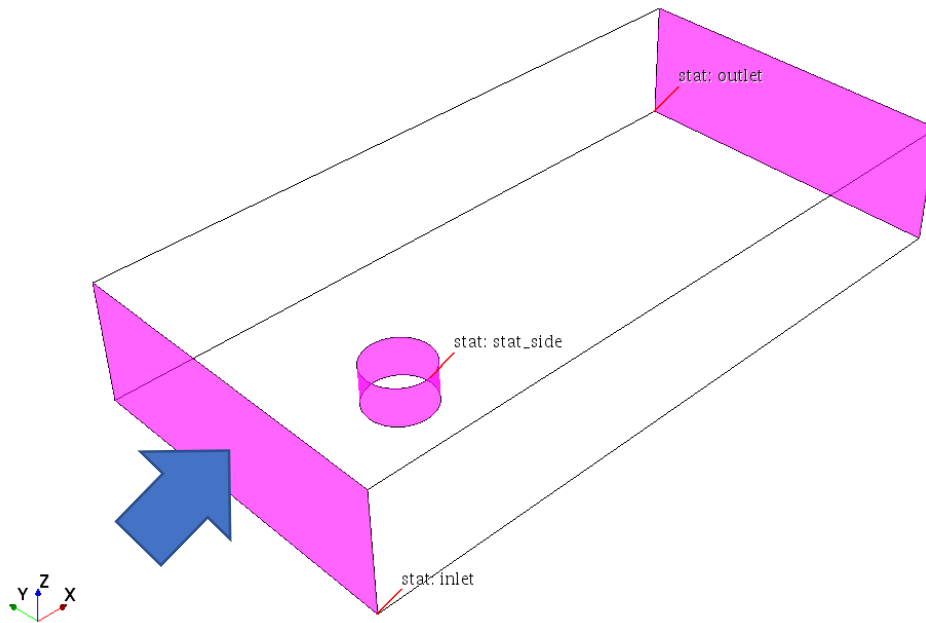


Figure 26 The position of inlet and outlet boundaries

The other surfaces on the cubic region are wall boundary conditions with slippery sides. This boundary condition means the flow is tangent to the surface. These surfaces are shown in Figure 27.

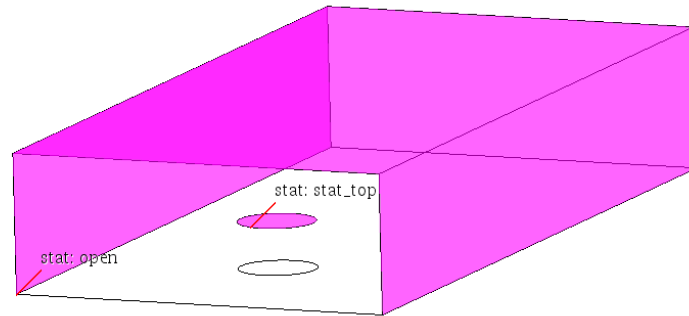


Figure 27 Open boundary conditions

The blade surface is set as a wall boundary condition with no-slip. This means the flow velocity is equal to zero on the blade surface. STAR-CCM+ calculates the torque that is generated on these surfaces.

3.3.3 Meshing

This subsection explains how the control volume is constructed in this thesis. The mesh is built to guarantee the simulation accuracy and to express the variation of geometric parameters.

To capture the flow separation, the first thickness of the boundary layer needs to satisfy $y^+ \sim 1$, because the *SST* $k - \omega$ turbulence model is applied. Furthermore, the growth rate should be at least 1.15. The growth rate indicates how cells grow compared with the next cell. The cell size increases as the cell is far from the blade surface shown in Figure 28. This rule is applied in the whole domain as shown in Figure 29. The mesh density is very thin around blades. The vertical plane from the inlet is illustrated as shown in Figure 30.

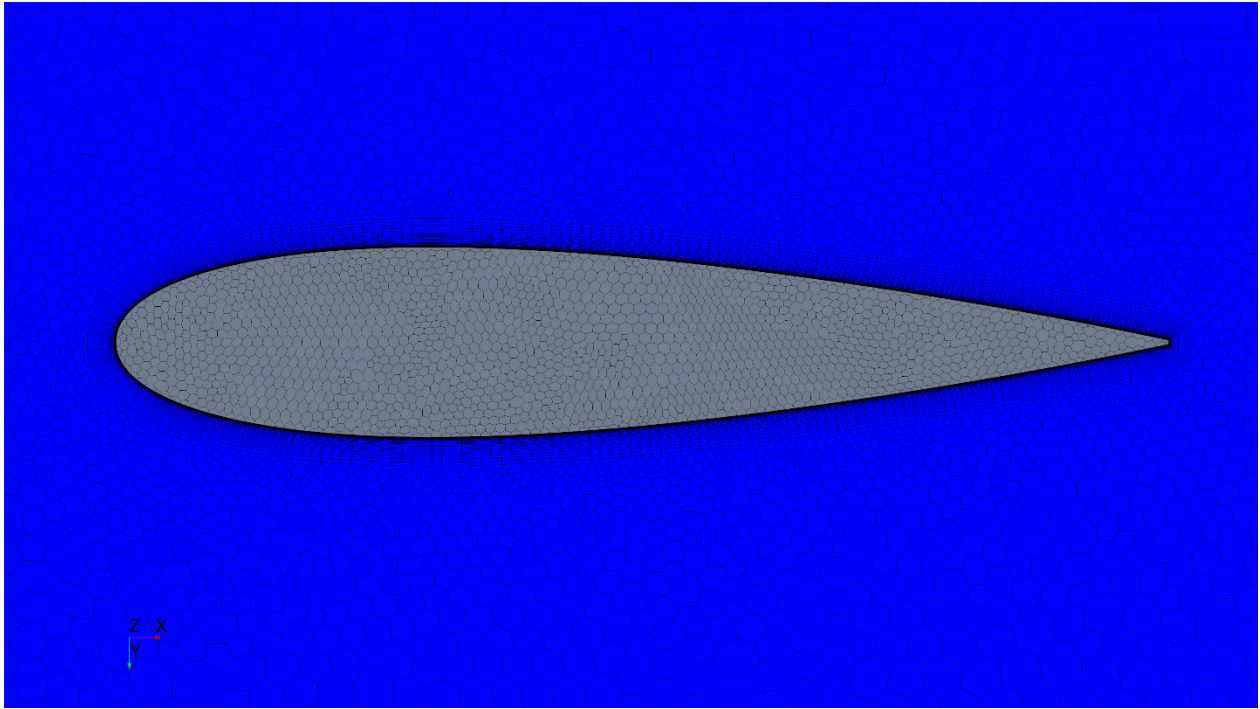


Figure 28 Mesh around the blade

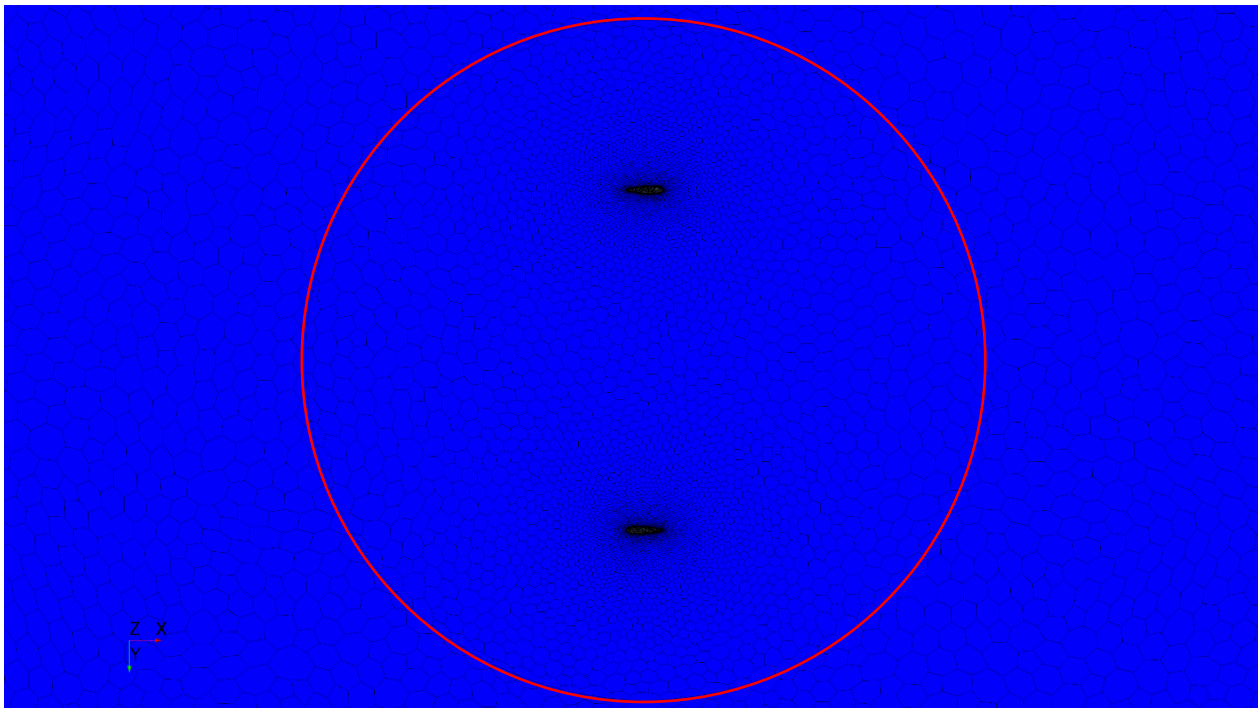


Figure 29 Rotating domain

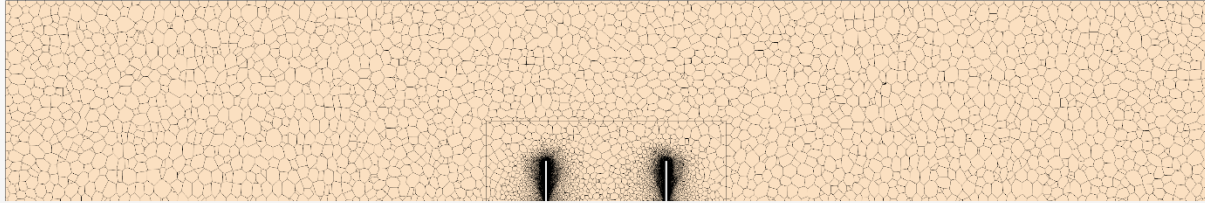


Figure 30 Vertical plane

As for the prism layer, it is refined to be divided as a boundary layer shown in Figure 31. The number of divisions is at least 15 and is adjusted from 15 to 35.

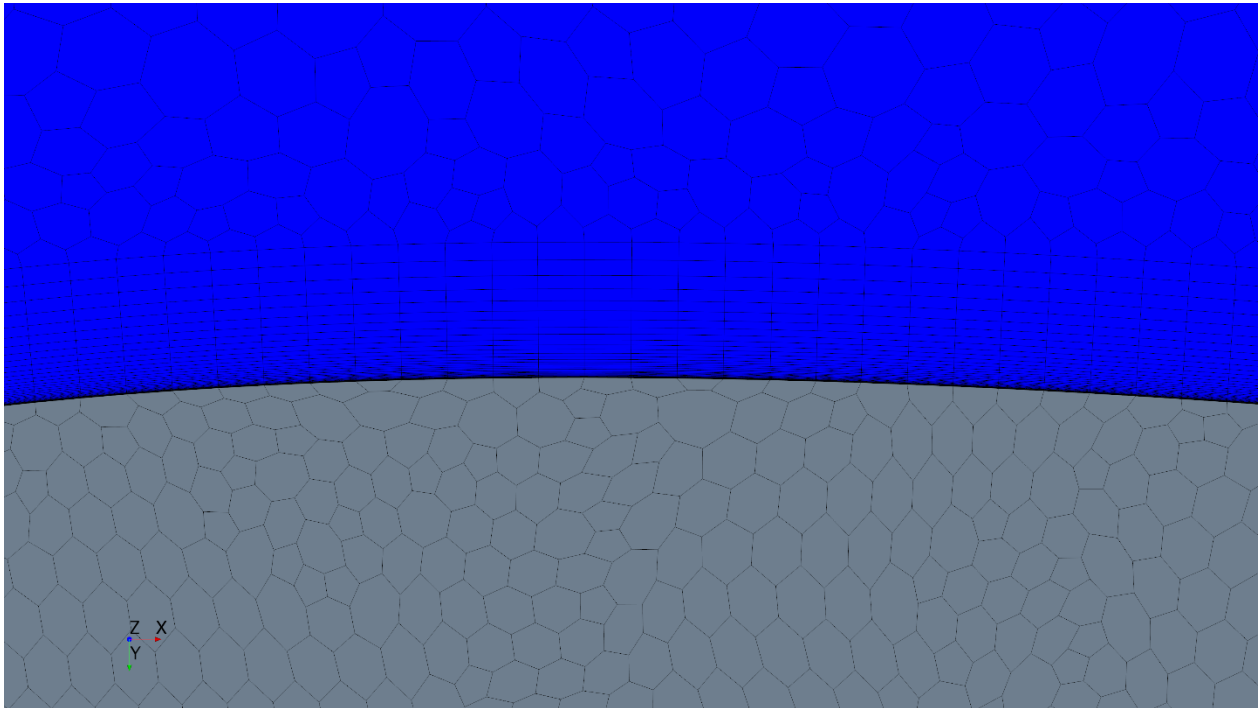


Figure 31 Prism layer

3.3.4 Cases

Six simulations of different turbines to be simulated have been identified and are listed in Table 7. The main geometric parameters for each referred case are reported. As discussed in the previous subsection, no shaft no arms cases are required. Six cases are determined by the following reasons.

- Case E is selected for comparison between original no shaft no arms case and our simulation.
- Case A, B, and C are selected to increase the number of no shaft no arms cases. These original cases have shaft.
- Case D and F are picked, because their turbulence models are different of $SST k - \omega$.

Recall that the focus is only the maximum power coefficient. So, the corresponding TSR for the maximum power coefficient is applied when simulating each case. These TSR values are extracted from the literature assuming that the C_p will pick for the same TSR even when the shaft and arms are removed.

Table 7 Employed Cases

Case	Original paper	D	L	c	N	Solidity	Wing section	TSR	Timestep
Case A	Case 2	2.5	3	0.4	3	0.152789	NACA0015	1.53	0.00107
Case B	Case 3	2	1.2	0.265	2	0.084352	NACA0021	2.3	0.00033
Case C	Case 5	1	1	0.06	2	0.038197	NACA0018	4.5	0.00016
Case D	Case 7	1.98	1.15	0.3	3	0.144686	NACA0021	1.35	0.00093
Case E	Case 10	0.75	0.5	0.08	2	0.067906	NACA0018	3	0.00059
Case F	Case 19	0.8	0.8	0.2	3	0.238732	NACA0021	1.25	0.00184

The numbers of cells for each simulation are listed on Table 8. Basically, the number of cells in the rotation region increases as the chord length is short. Because the mesh around blades needs to be more refined. For example, Figure 32 shows different sizes of cells' element in Case 3 around the leading edge. Instead of the thickness of boundary layer cells, the element length directly affects to the number of cells. The left side mesh element is 0.004 [m], and the right-side mesh element is 0.008 [m]. We explore with changing the element size to show the curvature around the leading edge.

Table 8 Number of cells

Case	Number of cells		
	All region	Rotation	Stationary
Case A	5,252,421	4,031,288	1,221,133
Case B	1,106,838	830,059	276,779
Case C	6,629,843	6,564,290	65,553
Case D	5,533,997	1,787,488	3,746,509
Case E	8,271,538	7,716,383	555,155
Case F	3,959,026	612,585	3,346,441

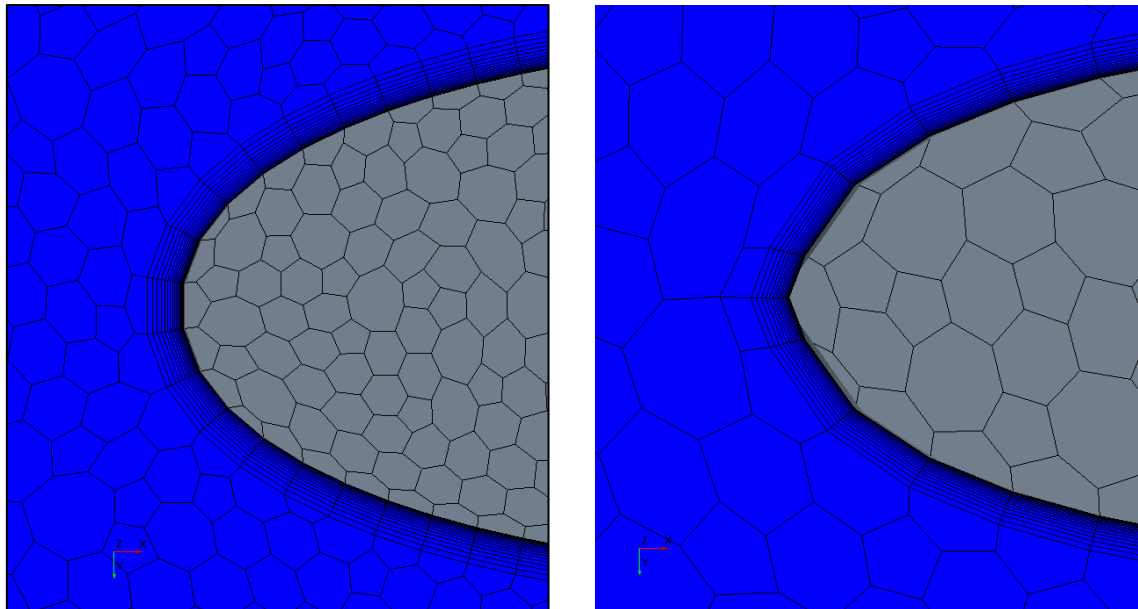


Figure 32 Mesh around the leading edge (Left:0.004m Right:0.008m)

The mesh around the blade for all cases are shown in from Figure 33 to Figure 38.

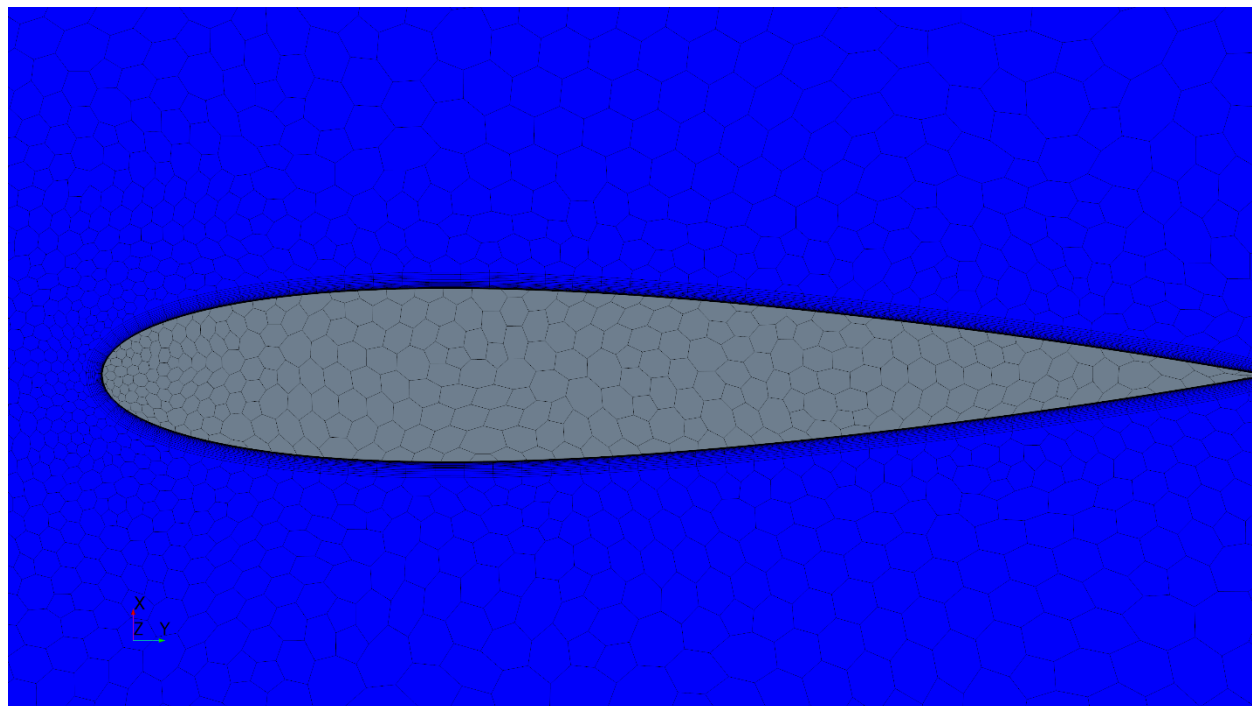


Figure 33 Case A mesh

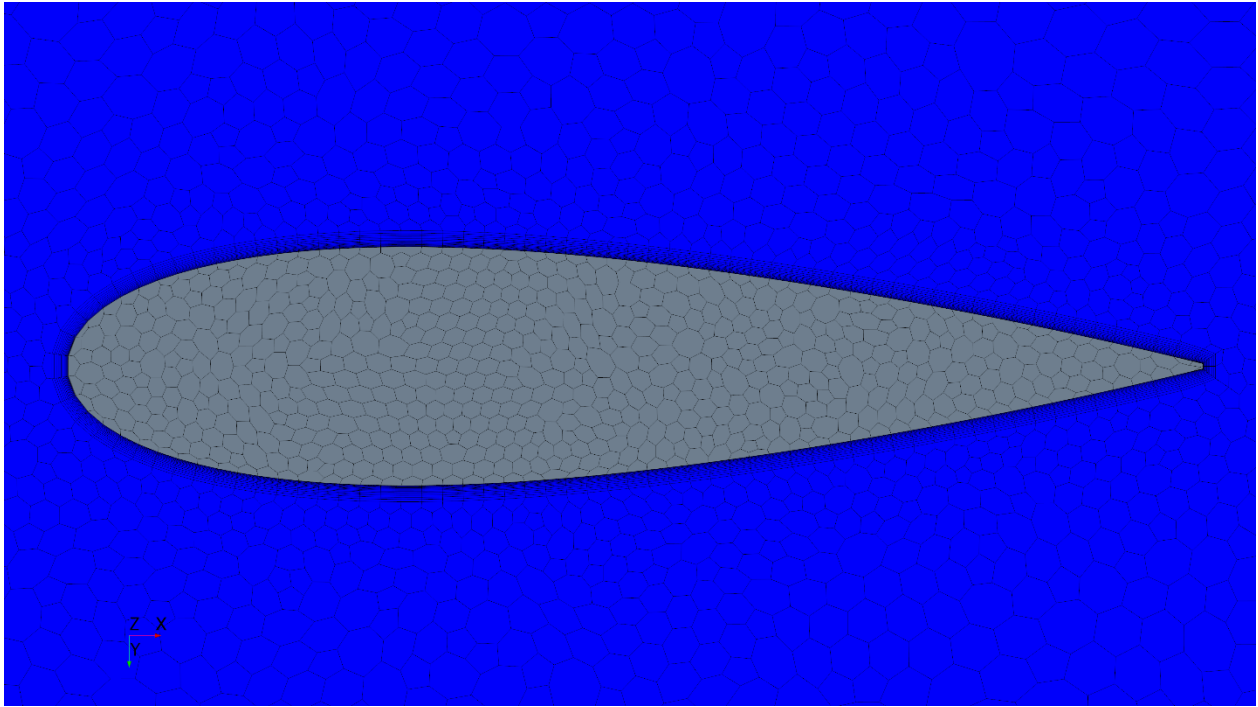


Figure 34 Case B mesh

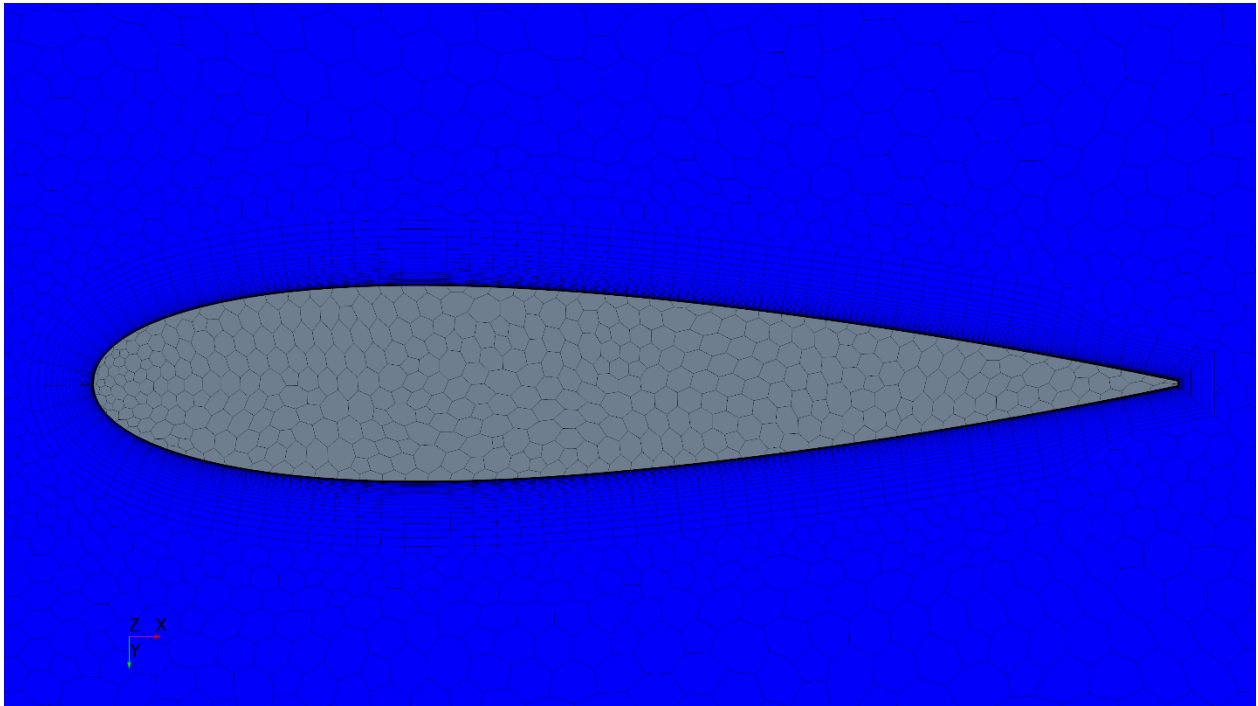


Figure 35 Case C mesh

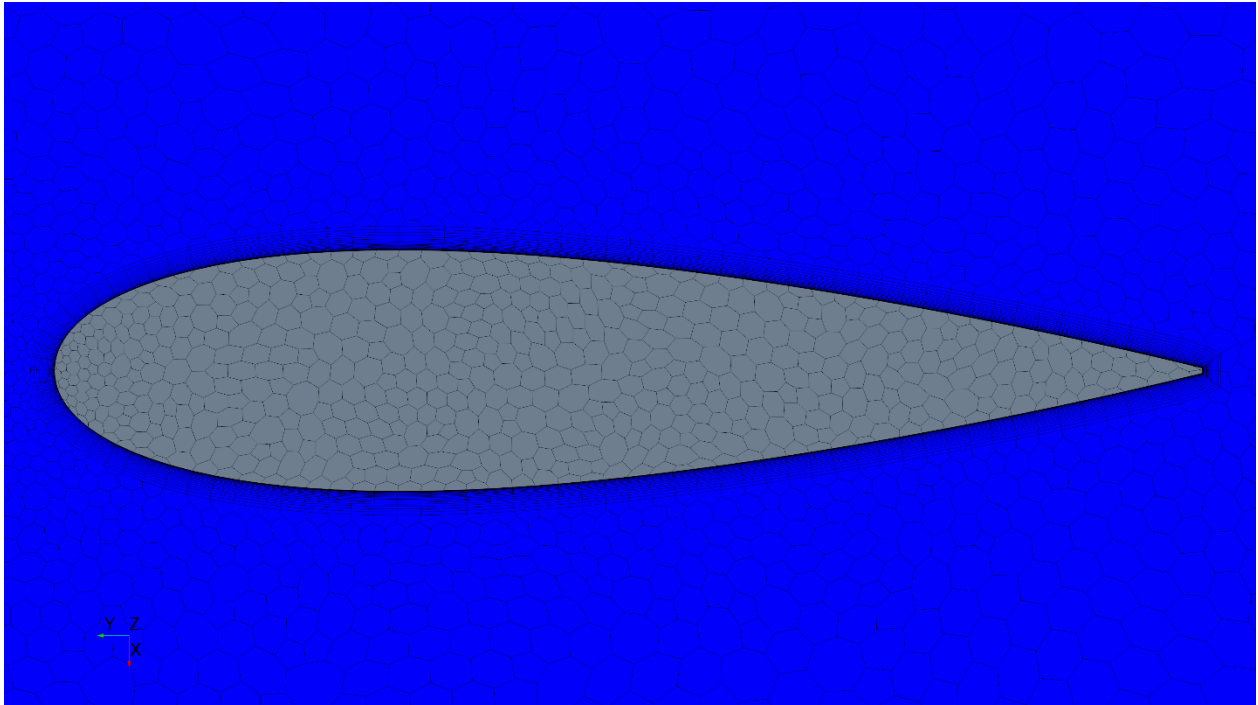


Figure 36 Case D mesh

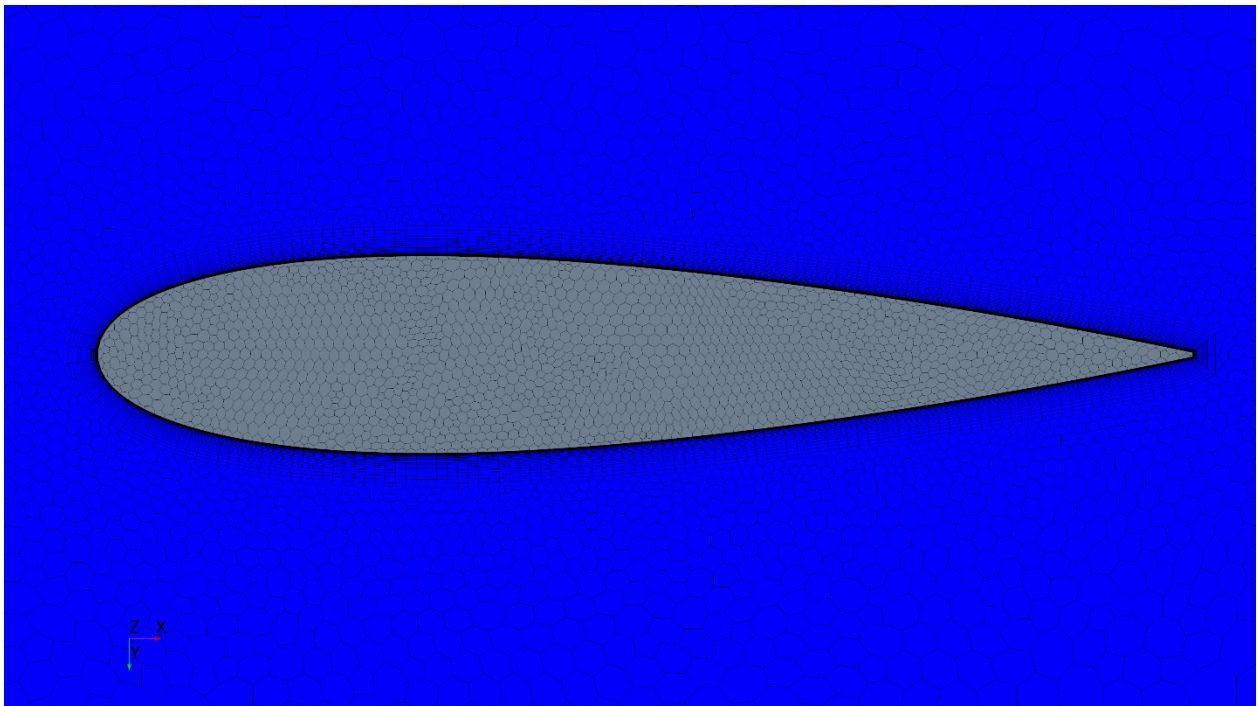


Figure 37 Case E mesh

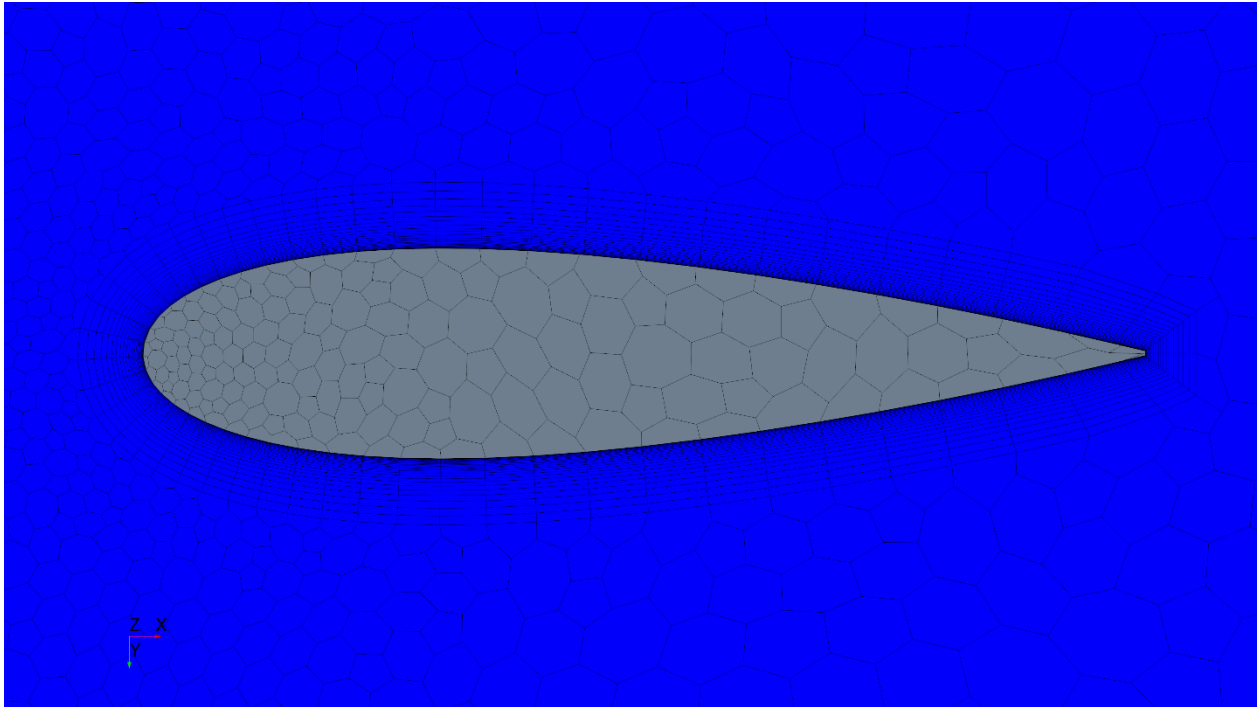


Figure 38 Case F mesh

3.3.5 Coordinates definition

The coordinate system is set as shown in Figure 39. The rotor center corresponds to the coordinate origin. The rotational axis corresponds to the z axis, and both x and y directions are perpendicular to the z direction. The rotational angle θ [-] is the counter-clockwise rotation. As the VAWT rotates, the rotational angle θ also increases.

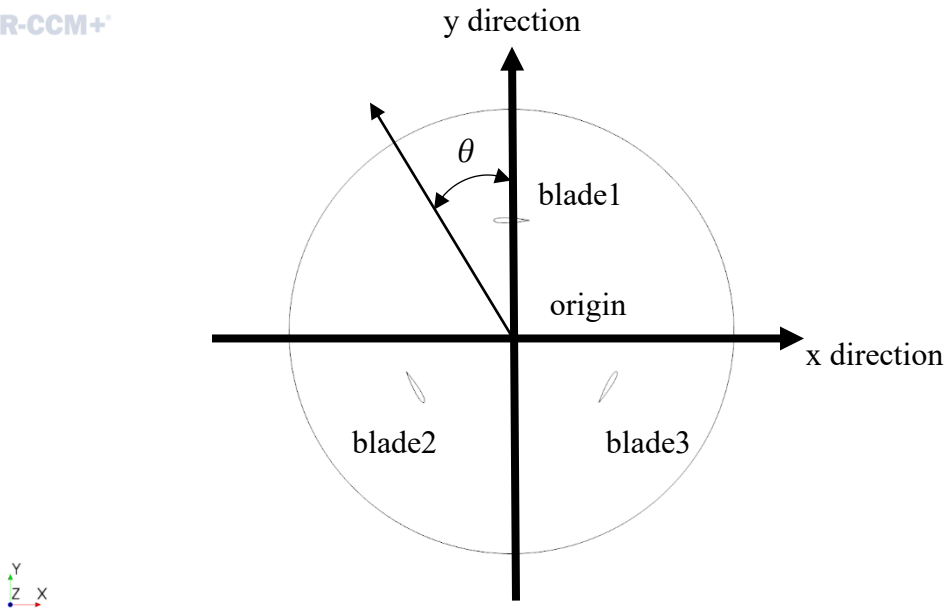


Figure 39 Coordinate system

3.3.6 Summary of geometry

Key geometries on each case are based on both the rotor diameter and blade length as shown in Figure 40. The rotating region has the double length of the rotor diameter and the blade length. The outer region is also based on the two lengths. Accordingly, it has a large buffer region.

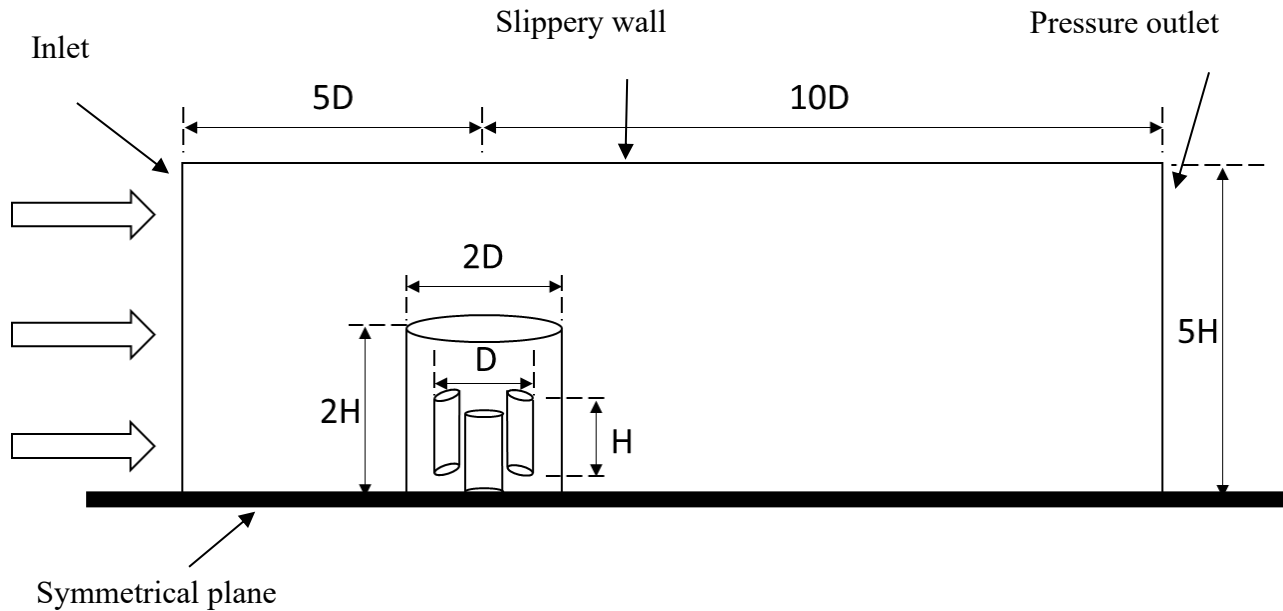


Figure 40 Summary of geometry

4 CFD Result

This chapter discusses the result of CFD performed on the cases identified earlier and compare the power coefficients calculated with the power coefficient from the original papers investigated as shown in Figure 42. Red bar chart shows the power coefficient that we investigated, and gray bar chart indicates the original power coefficient. The yellow line shows how many revolutions VAWT rotates from the initial condition. We also confirm that the temporal convergence of power coefficient between the present revolution and the previous revolution in each revolution is less than 1% as shown Table 9. Figure 43 to 48 show the power coefficient for each case for the last full revolution.

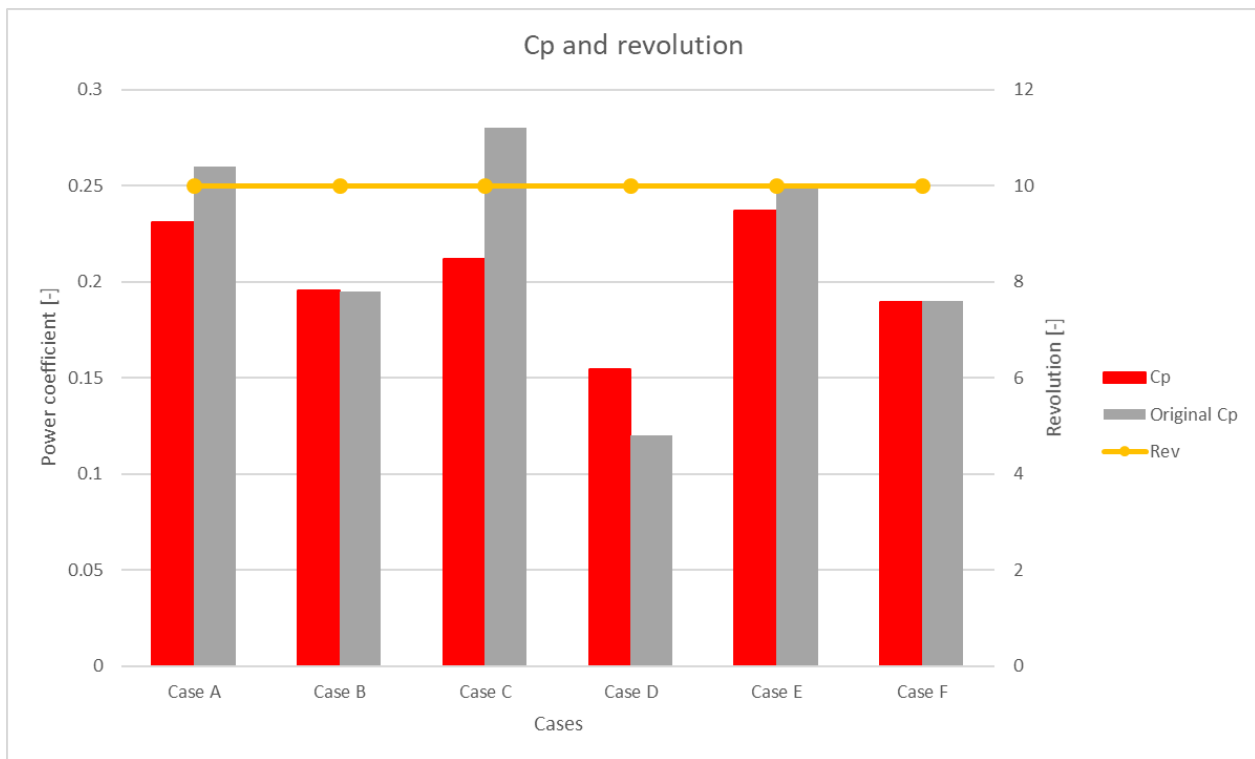


Figure 41 Result of power coefficient

Table 9 Simulation result

CaseID	Original paper	Original Cp	Simulated Cp	Difference	
				Last two cycles	Original to Simulation
Case A	Case2	0.26	0.230893	0.50%	10.52%
Case B	Case3	0.195	0.19575	0.03%	0.38%
Case C	Case5	0.28	0.211914	0.66%	24.32%
Case D	Case7	0.12	0.154736	0.15%	28.95%
Case E	Case10	0.25	0.237011	0.17%	5.20%
Case F	Case19	0.19	0.189469	0.51%	0.28%

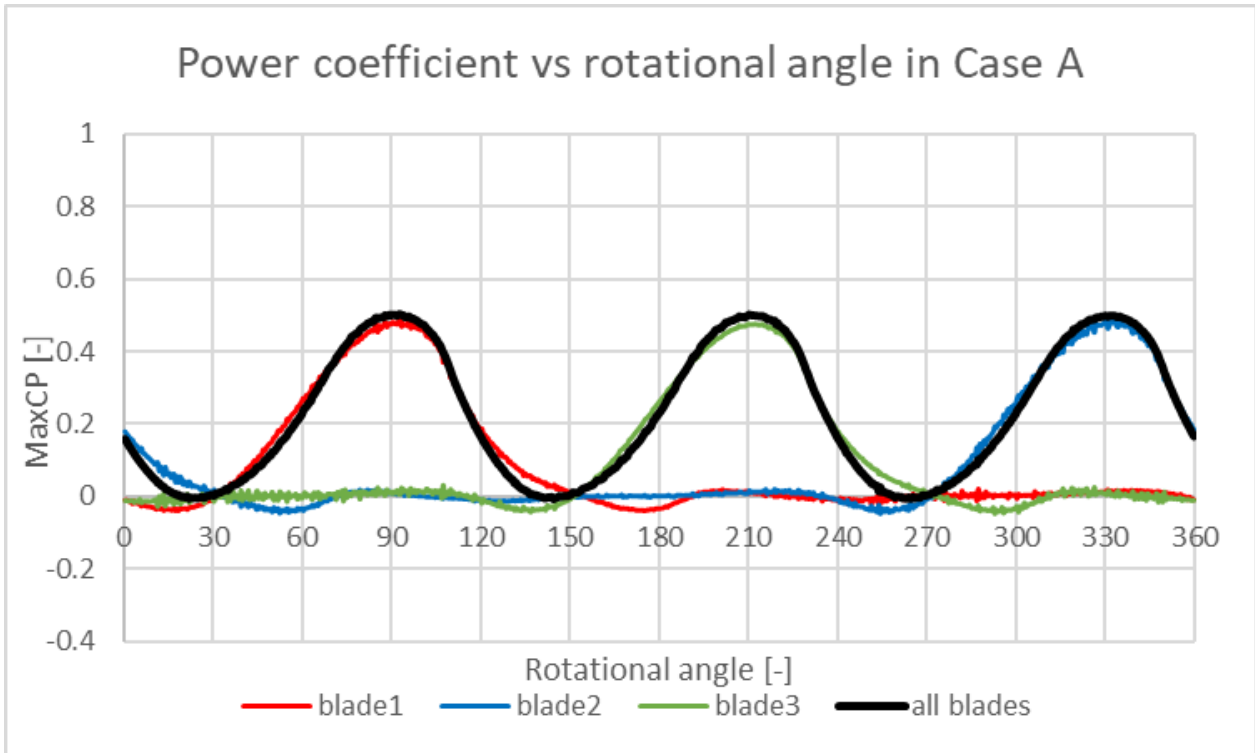


Figure 42 Power coefficient in case A

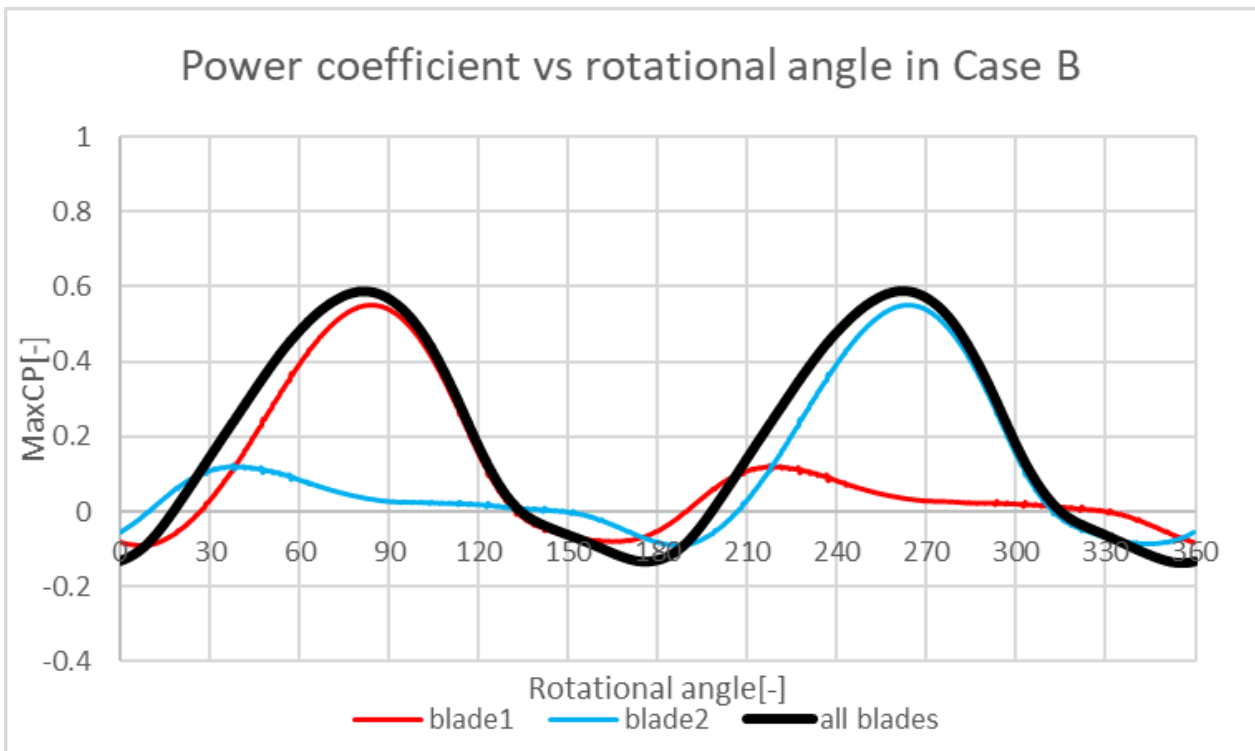


Figure 43 Power coefficient in case B

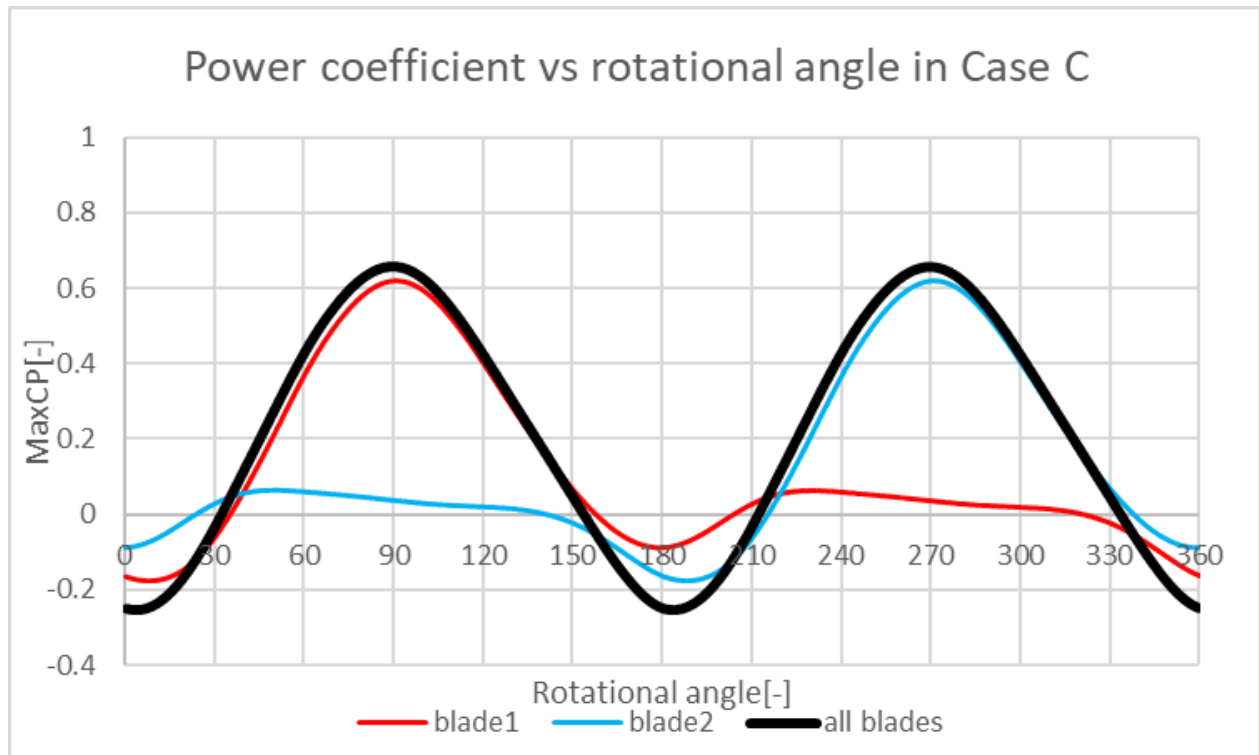


Figure 44 Power coefficient in case C

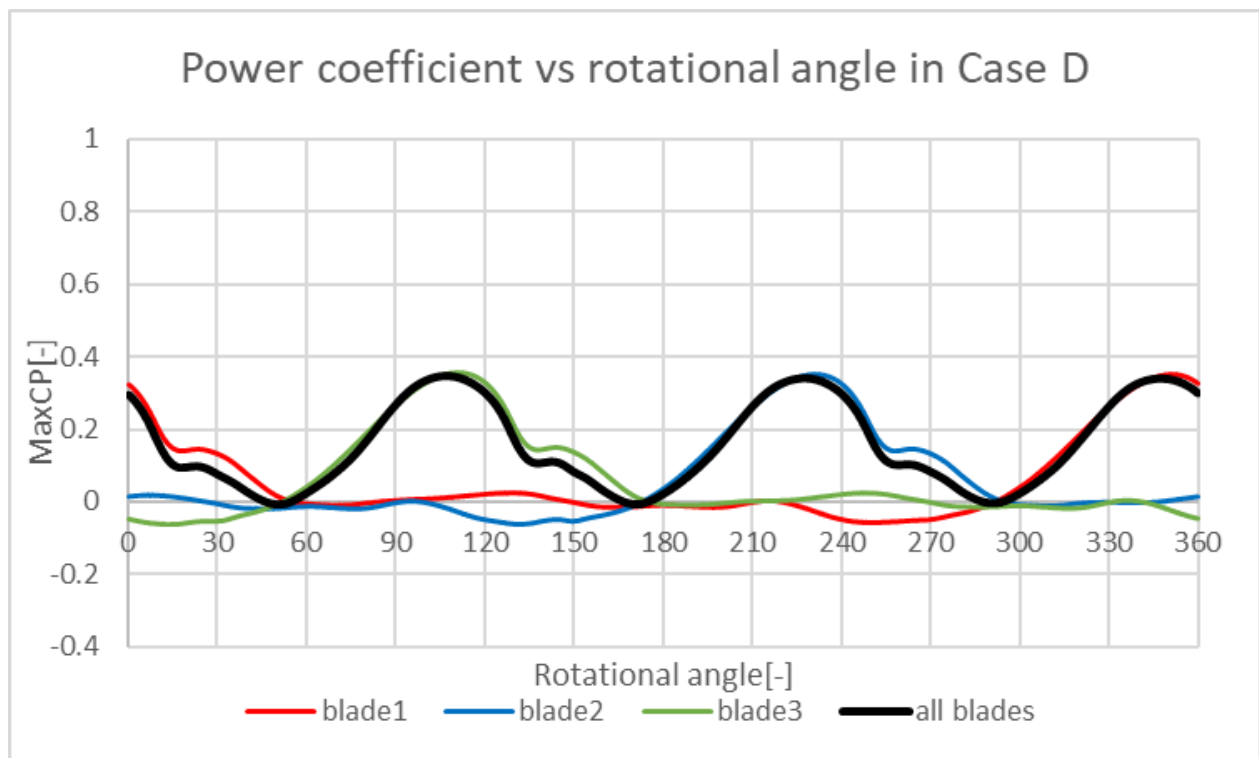


Figure 45 Power coefficient in case D

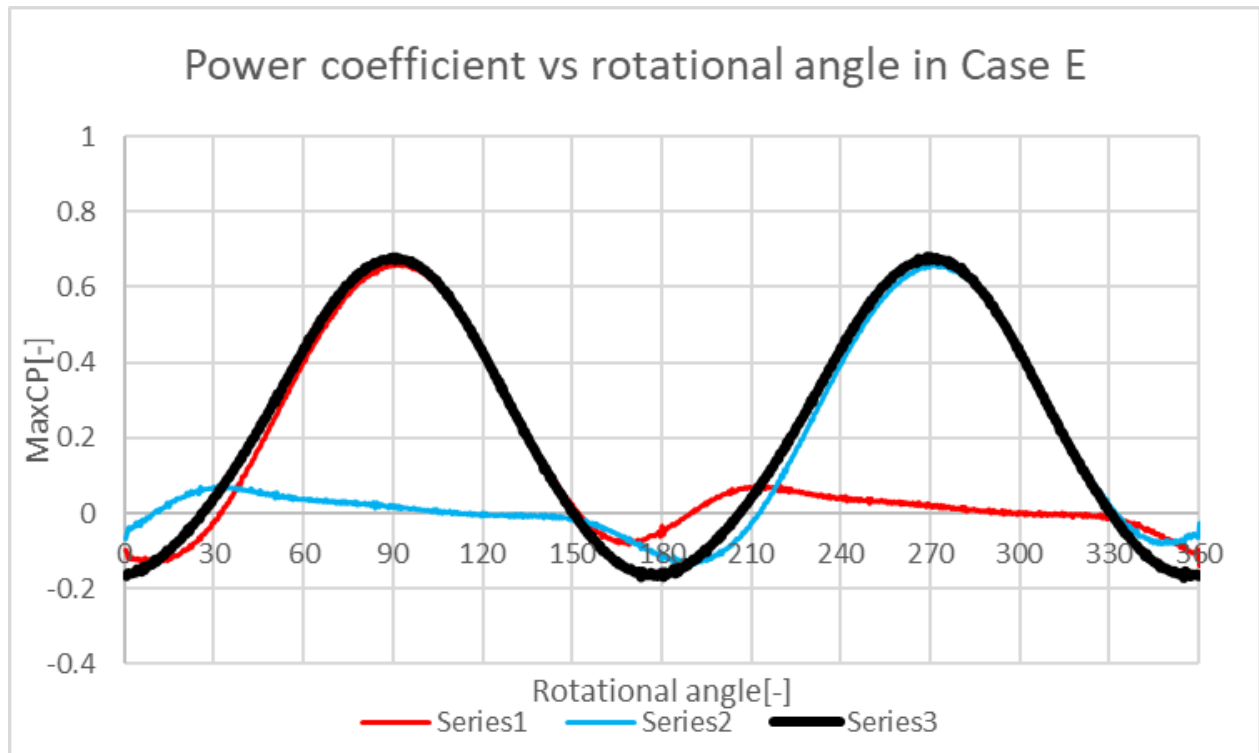


Figure 46 Power coefficient in case E

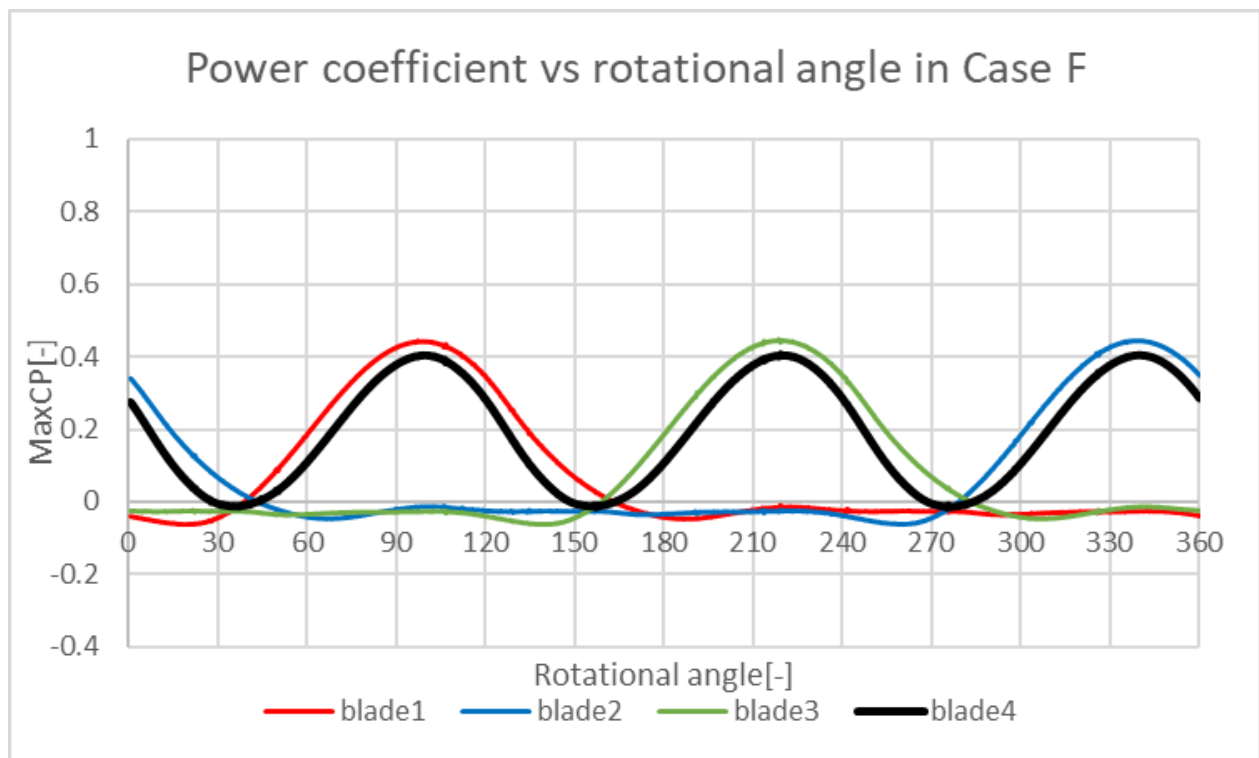


Figure 47 Power coefficient in case F

4.1 Vorticity

From Figure 48 to Figure 53 show vorticity fields. They show that these cases can capture the separation around blades in 10th revolutions.

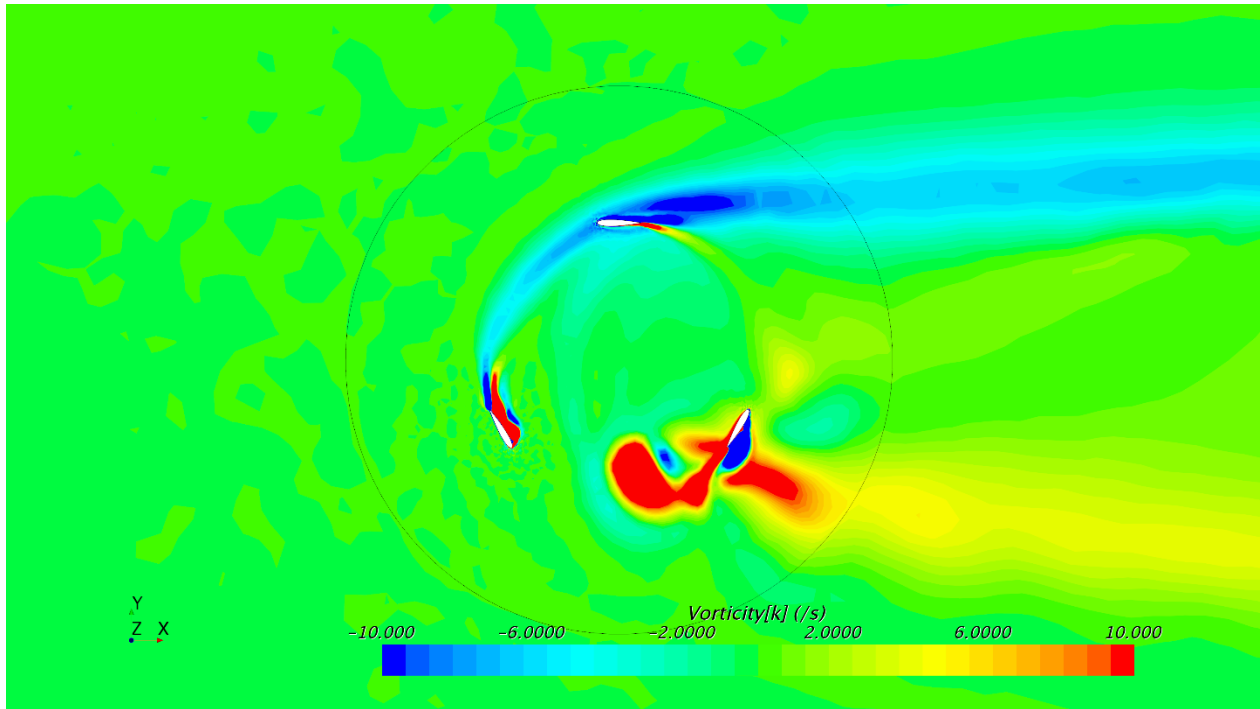


Figure 48 Case A vorticity rotation region

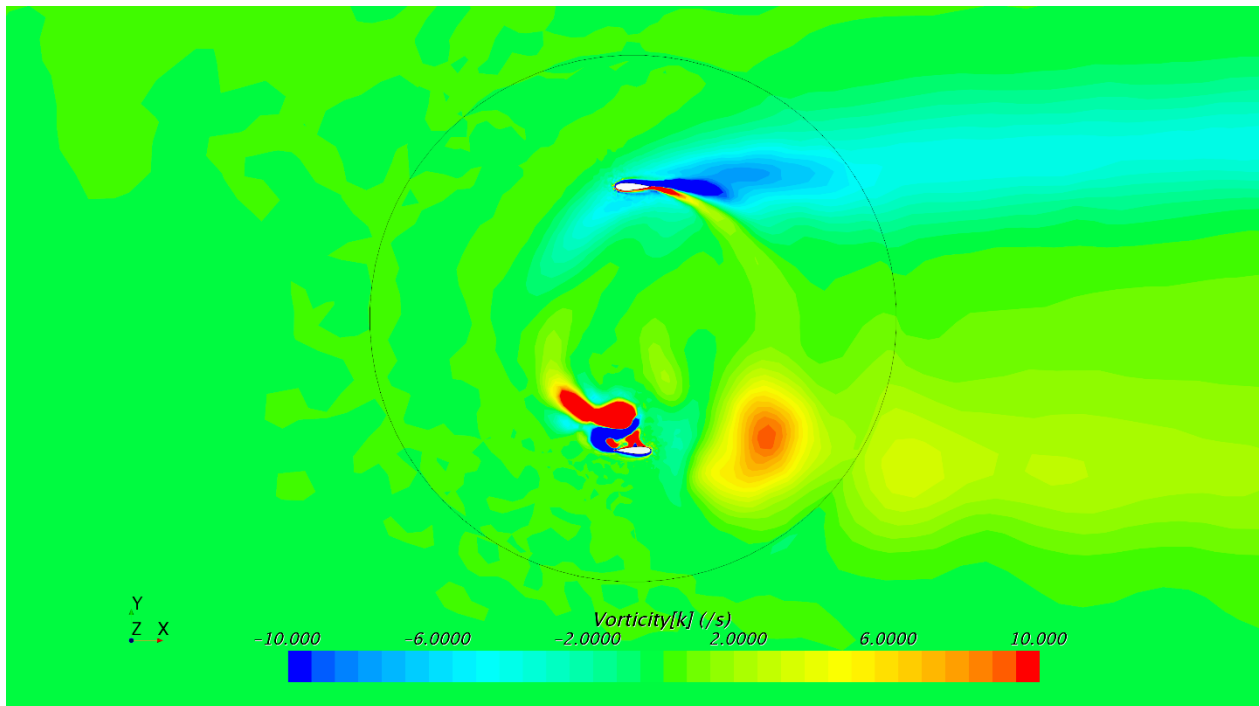


Figure 49 Case B vorticity rotation region

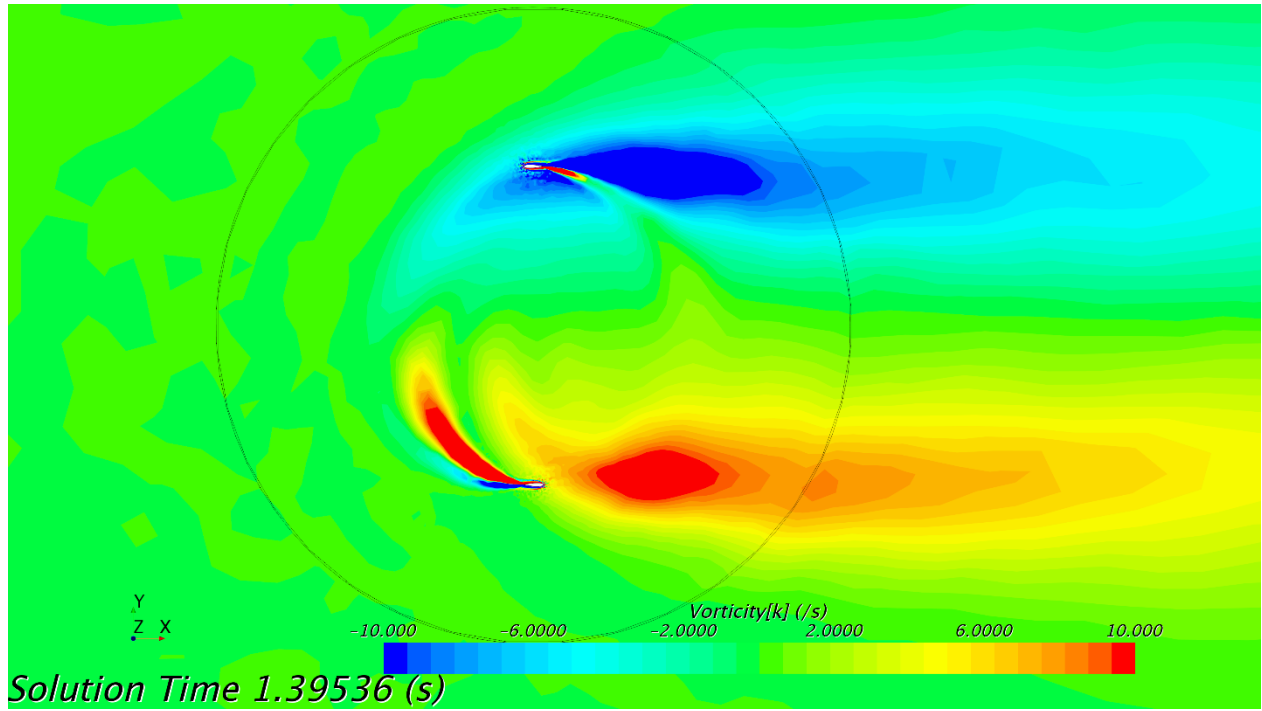


Figure 50 Case C vorticity rotation region

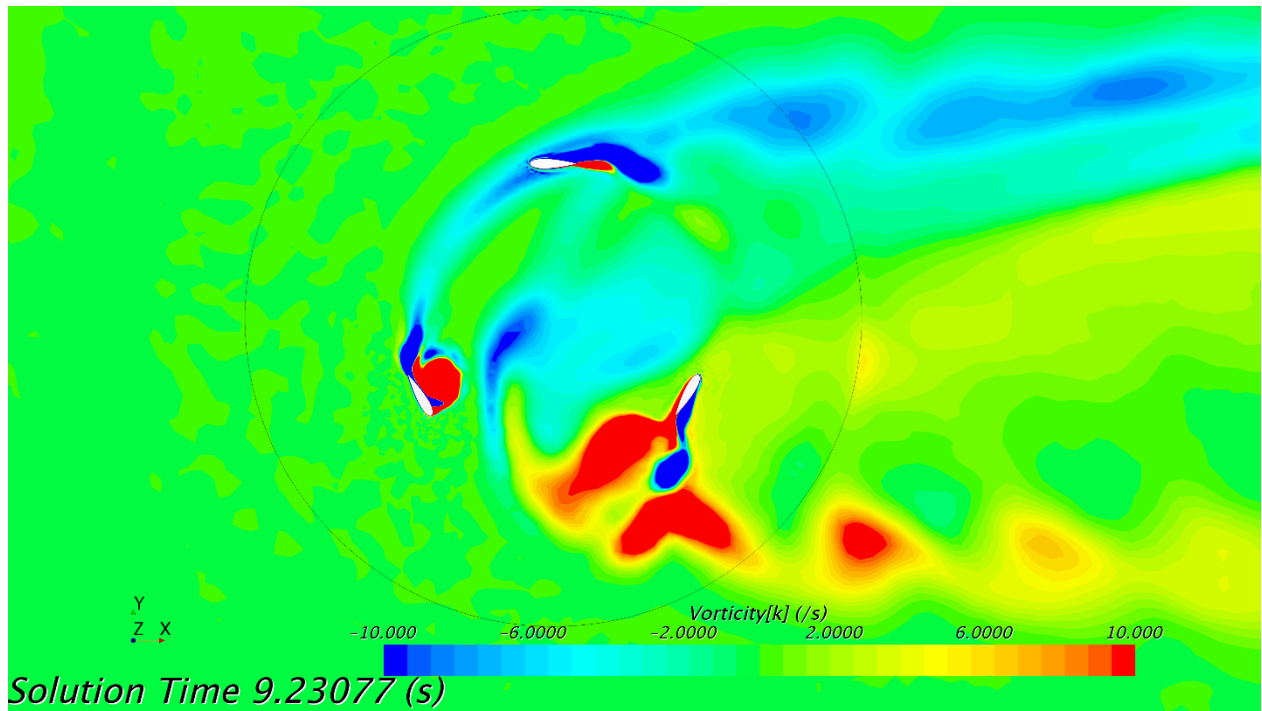


Figure 51 Case D vorticity rotation region

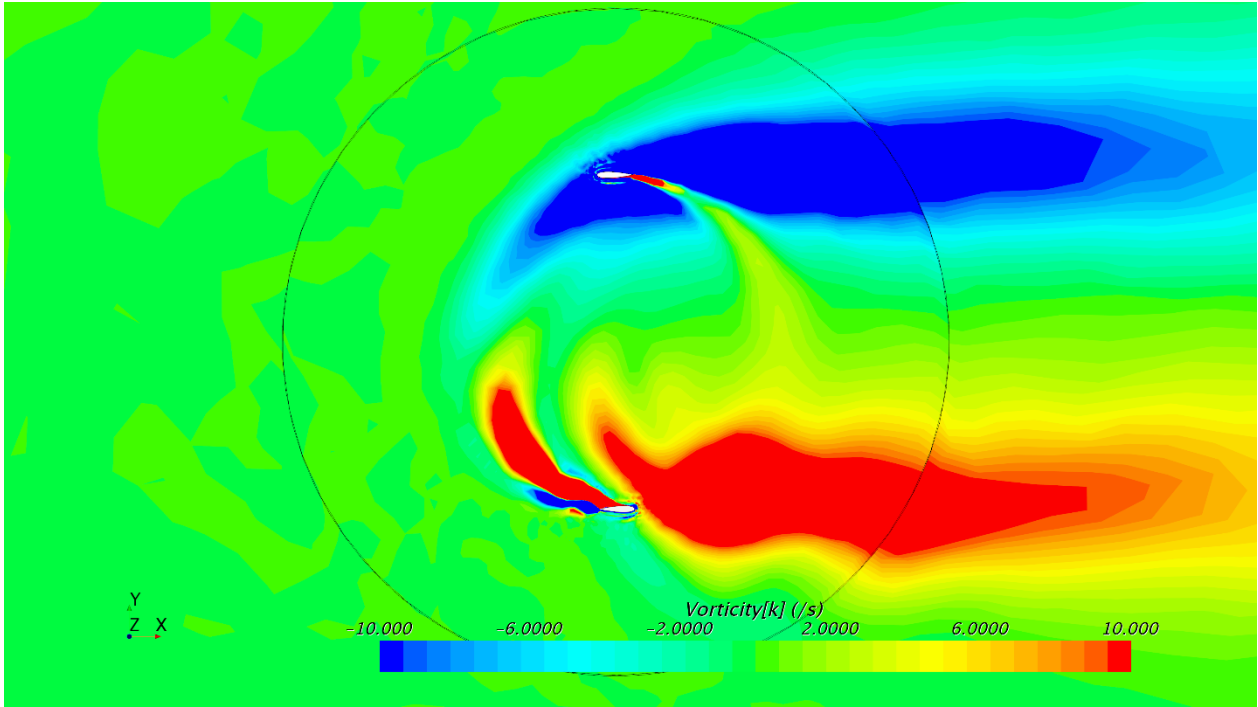


Figure 52 Case E vorticity rotation region

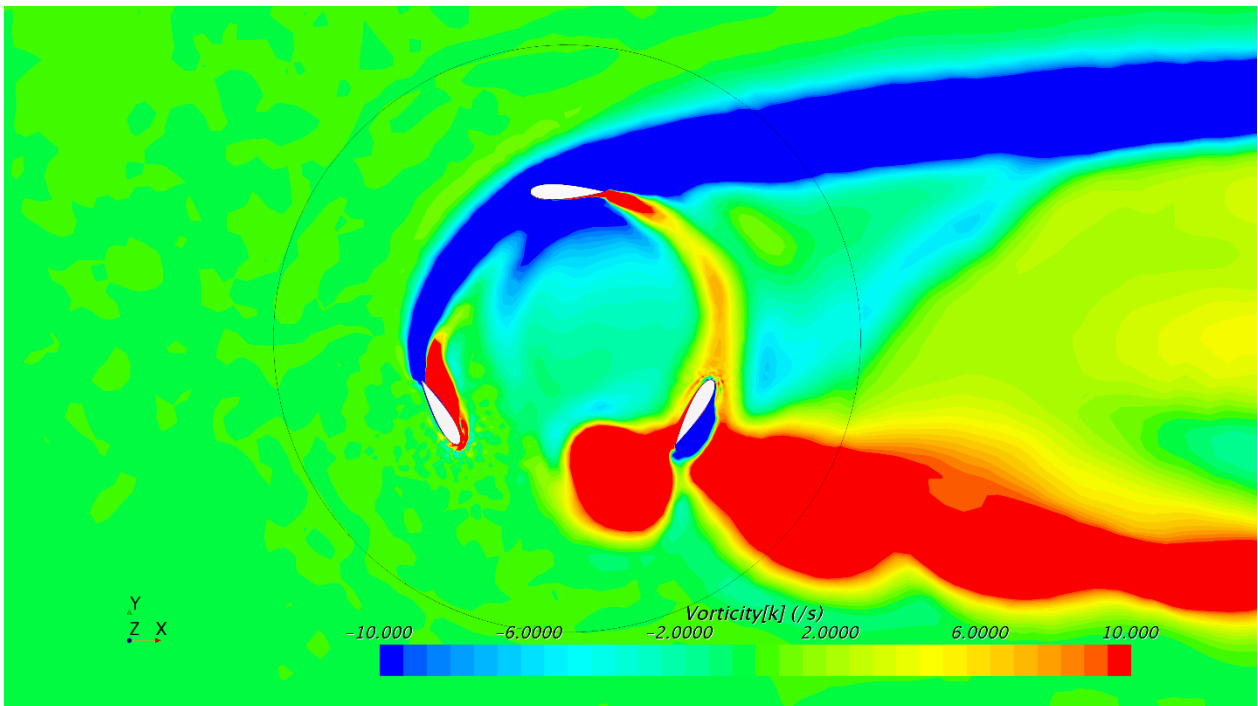


Figure 53 Case F vorticity rotation region

For the three blades cases, Case A, D, and F, we note that there is more vortex shedding. We also note that these cases have no the negative power coefficient compared to the two blades turbines from Figure 42 to Figure 47. This suggests that the three blades VAWT can provides the power continuously.

On the other hand, two blades VAWT has some rotation angle ranges that have the negative power coefficient. For example, from 150 to 195 of rotation angle in Case B cannot provides the generated power and the Case B type of VAWT rotates by the inertial moment during the negative power coefficient range.

4.2 Comparison to the original power coefficient

This section compares the different results from simulated case and the published values as shown in Table 10. The power coefficient of case F is close to the original power coefficient, and the difference is 0.28%. Similarly, power coefficients of cases B and E are also close. The difference is only 0.38% and 5.48%. Both these simulations employ the *SST k – ω* while case F used an LES in their simulation. Furthermore, the geometry is also different as some the published results have a shaft in the center of the rotor.

Table 10 Power coefficient comparison between my simulation and the published values

ID	Original Cp	Simulated Cp	Difference to original	Turbulence model	Supportive parts
CaseA	0.26	0.233	11.75%	SST k- ω	Shaft
CaseB	0.195	0.196	0.38%	SST k- ω	Shaft
CaseC	0.28	0.212	32.13%	SST k- ω	Shaft
CaseD	0.12	0.155	22.45%	k- ε	No
CaseE	0.25	0.237	5.48%	SST k- ω	No
CaseF	0.19	0.189	0.28%	LES	Shaft

In contrast, the difference related to case A, case C, and case D are relatively high. With regard to case D, the published results employ the *k – ε* turbulence model which may explain the underestimation for the power coefficient. In fact, it is the only case for which the calculated Cp with our methodology gave a higher value than in the published data. Clearly this is due to the k-epsilon model used which is known for not being very accurate. As for case A and case C, both of them have a relatively high inlet velocity boundary condition. For example, case 1 applies 9.0 [m/s] for the maximum power coefficient. Case C also applies 9.3 [m/s] for the experimental data. So, the difference of Reynolds number can affect their power coefficient.

To summarize, although there is some difference, these simulations are reliable in the statistical point of view. The coefficient of determination, R², is equal to 0.816 between the series of original Cp and the series of simulated Cp. The following chapter will present some model functions using values in literatures and values that we simulated in this chapter.

5 Data analysis and proposed models

As previously discussed, the projected area and aspect ratio, or both parameters that affect the power coefficient. First, it is observed that a large projected area and a large aspect ratio increase the power coefficient. This relationship is observed in Figure 18. Second, it was also noted that the thickness of the blade is very important. Considering these conditions, the following sections propose simple functions that can be used to predict the MaxCP without the need to run large CFD simulations.

5.1 Least squares method

This thesis applies a least squares method for a regression analysis. As for the regression, assuming the error as an objective function, the combination constants and intercepts that decreases the error is explored.

First, the objective function is defined as follows,

$$\epsilon_i = y_i - \alpha x_i - \beta_i \quad (5.1)$$

where ϵ_i is the error between the objective function and model function, y_i is the objective function, α_i is the constant, x_i is the independent variable, and β_i is the intercept. To evaluate the error as an absolute scale, ϵ_i is squared as follows.

$$\epsilon^2(\alpha, \beta)_i = \sum_i^n (y_i - \alpha x_i - \beta_i)^2 \quad (5.2)$$

Considering the error function is the minimum, partial derivative functions are equal to zero if the objective function is a linear function for both α_i and β_i . We get

$$\frac{\partial \epsilon(\alpha, \beta)_i}{\partial \alpha} = \frac{\partial \epsilon(\alpha, \beta)_i}{\partial \beta} = 0 \quad (5.3)$$

$$\alpha = \frac{\bar{x}\bar{y} - \bar{x} \cdot \bar{y}}{\bar{x}^2 - \bar{x}^2} \quad (5.4)$$

$$\beta = -\alpha\bar{x} + \bar{y} \quad (5.5)$$

The least squares methods can be applied for multiple function equation such as a polynomial function. This thesis examines model equations with t-test that.

5.2 t-test

Assuming a null hypothesis so that the objective function and explanatory variable are uncorrelated. t-test calculates a score of “t” that indicates how the variable is uncorrelated.

$$t_{score} = \frac{\beta}{SE_{\beta}} \quad (5.6)$$

where t_{score} is a score of “t”, and SE_{β} is a standard error of β . If the null hypothesis is true, t_{score} has a t-distribution with $n-2$ degrees of freedom.

$$SE_{\beta} = \frac{\sqrt{\frac{1}{n-2} \sum_i^n (y - y_i)^2}}{\sqrt{\sum_i^n (x - x_i)^2}} \quad (5.7)$$

$$t_{score} = \frac{\beta \sqrt{n-2}}{\sqrt{\frac{\varepsilon_i^2}{\sum_i^n (x - x_i)^2}}} \quad (5.8)$$

5.3 t-distribution and p-value

t-distribution is a derivative of a normal distribution. It is written as follows

$$f(t) = \frac{\Gamma\left(\frac{v+1}{2}\right)}{v\Gamma\left(\frac{v}{2}\right)} \left(1 + \frac{t^2}{v}\right)^{-\frac{v+1}{2}} \quad (5.9)$$

where v is a degrees of freedom, and Γ is a gamma function. As v increases to infinity, it approaches to the normal distribution. As for p-value, it denotes the probability that is on the t-distribution. Therefore, t_{score} is a reliability of the result of regression, and p-value is the probability of the reliability.

Applying to multiple regression model function, the term is terminated if t-stat doesn't satisfy t-distribution and p-value. After then, t-test is implemented again as t-stat satisfies t-distribution. This procedure determines the degrees of the model function and the fundamental term as shown in Figure 54. In this thesis, t-test applies 95% of significance.

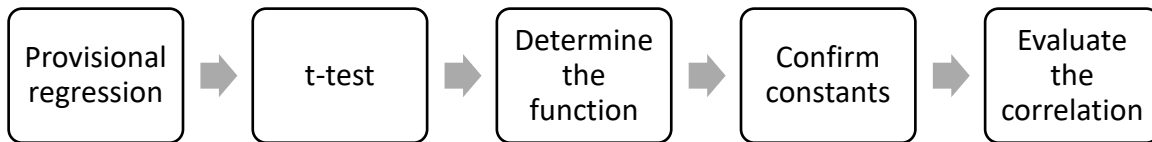


Figure 54 t-test procedure

5.4 Single parameter model function

This section explores what type of function can be a good approximation. First, we created trend lines by training cases. Training cases include no shaft no arms cases from literature and simulation that we conducted with $SST k - \omega$ turbulence model. The model function is compared with validation cases. Validation cases include no shaft no arms cases from literature based on $SST k - \omega$ turbulence model. Trend lines are generated by the function of Excel by Microsoft, and various types of approximation are applied: the linear approximation, the

exponential approximation, the logarithmic approximation, and the power approximation. Second, model equations provide model MaxCP. Third, calculating the coefficient of determination between validation cases and model MaxCP. If the coefficient of determination is low, a considerable model function is provided instead of the approximation equation.

The selected cases include the simulation cases performed in the previous chapter as shown in Table 11.

Table 11 Training cases

ID	Area	AR	Lambda	CP	H	D	N	c	Blade thickness
Case 9	2.40	4.5	2.3	0.160	1.2	2	2	0.265	21
Case 10	0.38	6.3	3	0.260	0.5	0.75	2	0.08	18
Case 12	7.50	7.5	1.5	0.280	3	2.5	3	0.4	15
Case 23	7.50	7.5	1.6	0.330	3	2.5	3	0.4	15
Case 24	0.64	4.0	1.3	0.190	0.8	0.8	3	0.2	18
Case A	7.50	7.5	1.53	0.233	3	2.5	3	0.4	15
Case B	2.40	4.5	2.3	0.196	1.2	2	2	0.265	21
Case C	1.00	16.7	4.5	0.212	1	1	2	0.06	18
Case D	2.28	3.8	1.348	0.155	1.15	1.98	3	0.3	21
Case E	0.38	6.3	3	0.237	0.5	0.75	2	0.08	18
Case F	0.64	4.0	1.25	0.189	0.8	0.8	3	0.2	21

In addition, validation cases are selected as cases with no shaft no arms cases from literatures as shown in Table 12.

Table 12 Validation cases

ID	Area	AR	Lambda	CP	H	D	N	c	Blade thickness
Case 6	2.40	4.5	2.245	0.17	1.2	2	2	0.265	21
Case 7	2.17	3.8	1.33	0.12	1.15	1.89	3	0.3	21
Case 8	2.40	4.5	2.3	0.18	1.2	2	2	0.265	21
Case 9	2.40	4.5	2.3	0.160	1.2	2	2	0.265	21
Case 10	0.38	6.3	3	0.26	0.5	0.75	2	0.08	18
Case 12	7.5	7.5	1.5	0.28	3	2.5	3	0.4	15
Case 17	8.1	7.1	2.2	0.373	3	2.7	2	0.42	15
Case 18	8.1	7.1	2	0.334	3	2.7	3	0.42	15
Case 20	0.24	4.0	1.8	0.22	0.4	0.6	2	0.1	22
Case 22	2.40	4.5	2.2	0.2	1.2	2	2	0.265	21
Case 23	7.50	7.5	1.6	0.330	3	2.5	3	0.4	15
Case 24	0.64	4.0	1.3	0.190	0.8	0.8	3	0.2	18
Case 28	0.74	9.6	2.6	0.3247	1.434	0.515	3	0.15	18

Model functions are provided by the creating trend lines. Excel by Microsoft ltd., provides some trend lines with various types of functions such as exponential, linear, logarithmic, or power functions. Suggested functions are evaluated by the coefficient of determine between them and validation cases' MaxCP. The difference is between MaxCP for validation cases and simulated power coefficient as shown in Table 13. The linear function is applied because of the largest coefficient of determination.

Table 13 Trend line functions for blade thickness

	Exponential		Linear		Logarithmic		Power	
	CP	Difference	CP	Difference	CP	Difference	CP	Difference
Case 6	0.174	-2%	0.175	-3%	0.176	-4%	0.174	-2%
Case 7	0.174	-45%	0.175	-46%	0.176	-47%	0.174	-45%
Case 8	0.174	3%	0.175	3%	0.176	2%	0.174	3%
Case 9	0.174	-9%	0.175	-9%	0.176	-10%	0.174	-9%
Case 10	0.227	13%	0.224	14%	0.219	16%	0.227	13%
Case 12	0.279	0%	0.281	0%	0.282	-1%	0.279	0%
Case 17	0.279	25%	0.281	25%	0.282	24%	0.279	25%
Case 18	0.279	16%	0.281	16%	0.282	16%	0.279	16%
Case 20	0.156	29%	0.160	27%	0.165	25%	0.156	29%
Case 22	0.174	13%	0.175	12%	0.176	12%	0.174	13%
Case 23	0.279	15%	0.281	15%	0.282	15%	0.279	15%
Case 24	0.227	-19%	0.224	-18%	0.219	-15%	0.227	-19%
Case 28	0.227	30%	0.224	31%	0.219	33%	0.227	30%
R2	0.675		0.682		0.566		0.665	

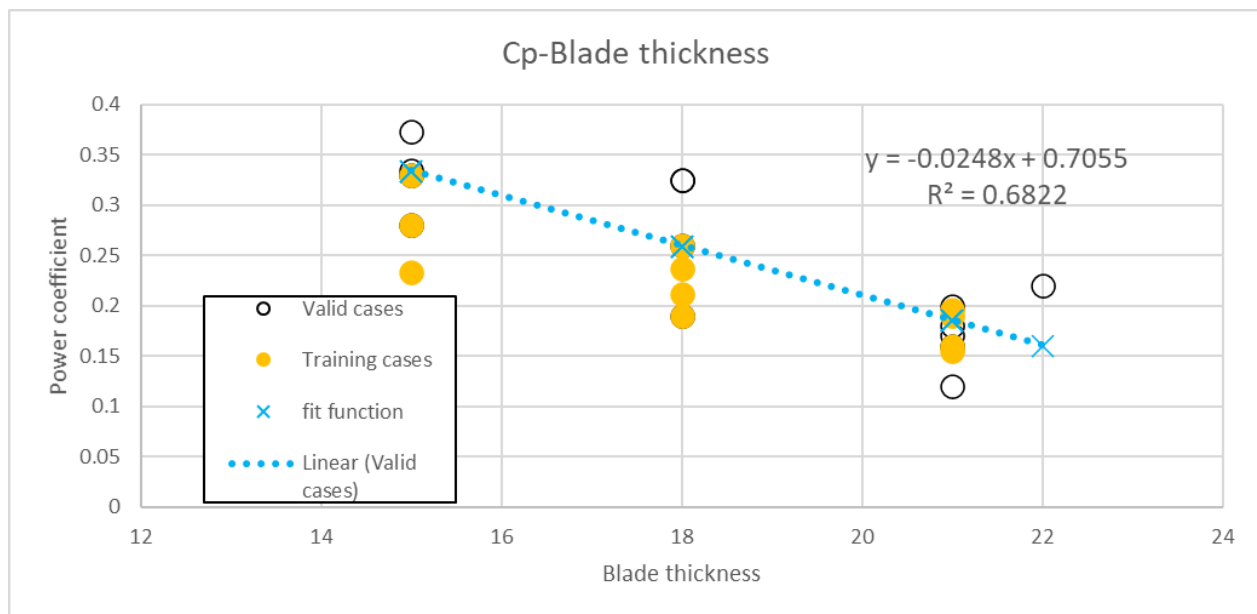


Figure 55 Fit function of the blade thickness

Similar to the model function of blade thickness, a model function for the aspect ratio is created. The trend line of the model function of aspect ratio is generated and matches to validation cases as shown in Figure 56 and Table 14. The coefficient of determination between this model function to validation cases is 0.786. Note that Case C is removed because it has a relatively high aspect ratio.

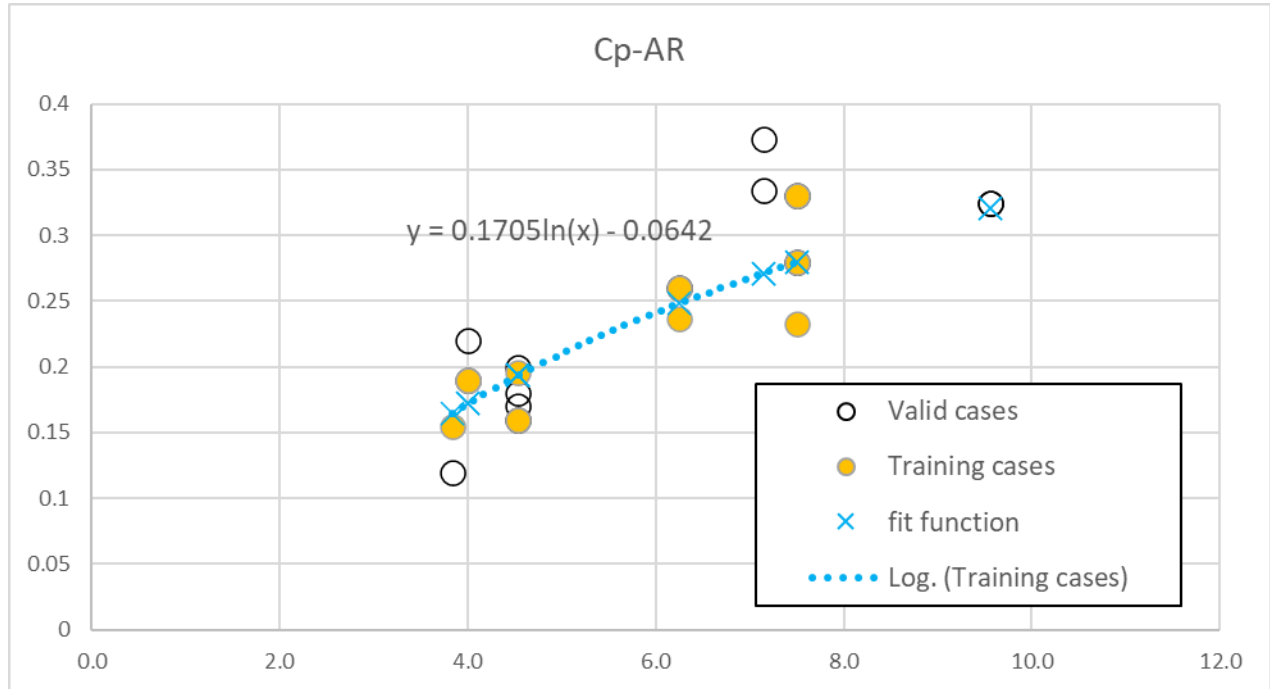


Figure 56 Fit function of aspect ratio

Table 14 Trend line functions for aspect ratio

	Exponential		Linear		Logarithmic		Power	
	CP	Difference	CP	Difference	CP	Difference	CP	Difference
Case 6	0.188	-10%	0.190	-12%	0.193	-14%	0.190	-12%
Case 7	0.171	-42%	0.169	-40%	0.165	-37%	0.167	-40%
Case 8	0.188	-4%	0.190	-6%	0.193	-7%	0.190	-6%
Case 9	0.188	-17%	0.190	-19%	0.193	-21%	0.190	-19%
Case 10	0.238	9%	0.243	6%	0.248	5%	0.243	7%
Case 12	0.282	-1%	0.282	-1%	0.279	0%	0.279	0%
Case 17	0.269	28%	0.271	27%	0.271	27%	0.269	28%
Case 18	0.269	20%	0.271	19%	0.271	19%	0.269	20%
Case 20	0.174	21%	0.174	21%	0.172	22%	0.173	21%
Case 22	0.188	6%	0.190	5%	0.193	3%	0.190	5%
Case 23	0.282	14%	0.282	15%	0.279	15%	0.279	15%
Case 24	0.174	8%	0.174	9%	0.172	9%	0.173	9%
Case 28	0.375	-15%	0.346	-6%	0.321	1%	0.335	-3%
R2	0.685		0.748		0.787		0.760	

In summary, two types of model functions are suggested and evaluated in this section. Both of them show a correlation to validation cases. The model function of aspect ratio has the larger coefficient of determination than the projected area's one.

5.5 Multiple parameters model functions

This section provides some model equations of multiple parameters with a multiple regression analysis. In the previous section, the trend line for MaxCP to blade thickness is based on non-linear function, and the trend line for MaxCP to aspect ratio is based on linear function, respectively.

The multiple regression analysis has a shape that is shown as follows,

$$Y = a_1x_1 + a_2x_2 + c1 \quad (5.10)$$

$$Y = a_1x_1 + a_2x_2 + a_3x_1x_2 + c1 \quad (5.11)$$

$$Y = a_1x_1 + a_2x_2 + a_3x_1^2 + a_4x_2^2 + c1 \quad (5.12)$$

a_n is arbitrary constant, c_1 is the intercept, and x_n is a variable for function of Y . In this case, $x_1 = \text{blade thickness}$, and $x_2 = \text{aspect ratio}$.

5.5.1 Result

The result of multiple regression is shown as follows. Overall, all predicted variables have small t-stat value, so suggested model functions don't fit to this problem. From (5.10) to (5.12) are plugged these variables, we get

$$Y = -0.00515x_1 + 0.0231x_2 + 0.188 \quad (5.13)$$

$$Y = -0.0144x_1 - 0.00642x_2 + 0.00170x_1x_2 + 0.354 \quad (5.14)$$

$$Y = 0.0711x_1 - 0.0128x_2 - 0.00199x_1^2 + 0.00376x_2^2 - 0.453 \quad (5.15).$$

Accordingly, MaxCP that is predicted by these models are shown as follows.

Table 15 Result of multiple regression

Candidate	R square to validation cases	Variables	Coefficients	Standard Error	t Stat	P-value
Candidate1	81.5%	a1	-0.00515	0.00900	-0.571	0.586
		a2	0.0231	0.0151	1.54	0.168
		Intercept c1	0.188	0.244	0.770	0.466
Candidate2	79.2%	a1	-0.0144	0.0261	-0.551	0.601
		a2	-0.00642	0.0792	-0.0811	0.938
		a3	0.00170	0.00446	0.381	0.716
		Intercept c1	0.354	0.508	0.697	0.512
Candidate3	61.8%	a1	0.0711	0.316	0.225	0.831
		a2	-0.0128	0.326	-0.0393	0.970
		a3	-0.00199	0.00799	-0.249	0.813
		a4	0.00376	0.0324	0.116	0.912
		Intercept c1	-0.453	2.39	-0.189	0.857

Table 16 Prediction results

Case	Candidate1		Candidate2		Candidate3	
	CP	Difference	CP	Difference	CP	Difference
Case 6	0.184	8.5%	0.184	8.4%	0.181	6.3%
Case 7	0.168	40.3%	0.164	36.6%	0.168	39.8%
Case 8	0.184	2.5%	0.184	2.4%	0.181	0.4%
Case 9	0.184	15.3%	0.184	15.2%	0.181	13.0%
Case 10	0.240	-7.8%	0.246	-5.3%	0.248	-4.5%
Case 12	0.284	1.4%	0.281	0.5%	0.281	0.3%
Case 17	0.276	-26.1%	0.275	-26.4%	0.266	-28.7%
Case 18	0.276	-17.4%	0.275	-17.8%	0.266	-20.4%
Case 20	0.167	-24.0%	0.161	-26.7%	0.156	-29.1%
Case 22	0.184	-7.8%	0.184	-7.8%	0.181	-9.6%
Case 23	0.284	-13.9%	0.281	-14.7%	0.281	-14.9%
Case 24	0.188	-1.2%	0.192	0.9%	0.190	0.2%
Case 28	0.316	-2.6%	0.326	0.5%	0.403	24.0%

The most correlated and predictable model function is Candidate 2. Although it has a low score in t-test, Candidate 2 has the smallest difference in these model functions. It is clearly showed that the characteristics decreasing MaxCP as blade thickness increases in the lower aspect ratio range. Moreover, the higher MaxCP are likely to be predicted well for using Candidate 2. The maximum difference in this model is about 36.6%. Though it appears large this is not surprising for Cp predictions. Recall that in Chapter 3 the CFD results for case D were 29% different from other results in the literature.

From Figure 57 to show surfaces illustrating the model equations. The horizontal axes are both blade thickness and aspect ratio, and the vertical axis is MaxCP, respectively.

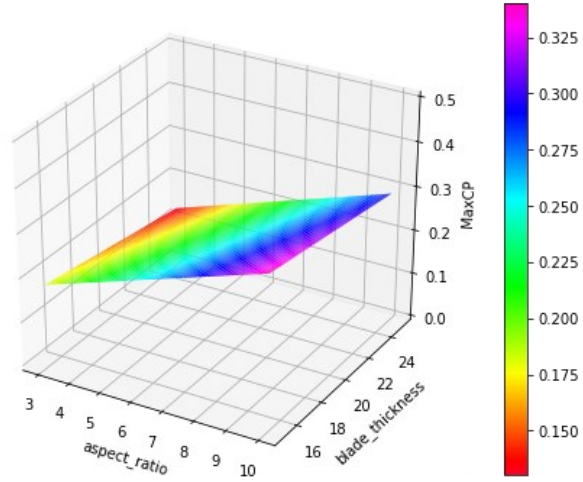


Figure 57 Candidate 1 model equation plane

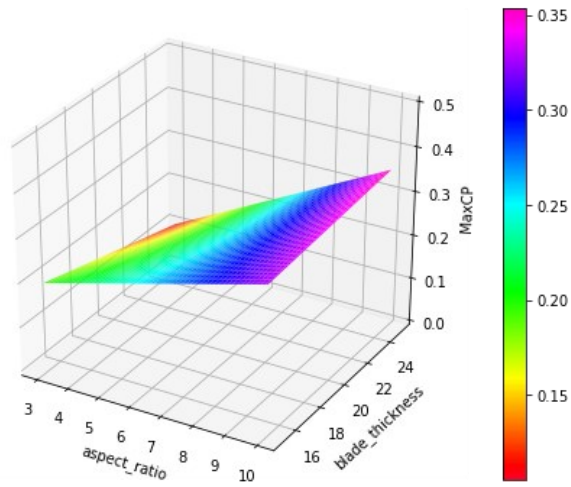


Figure 58 Candidate 2 model equation plane

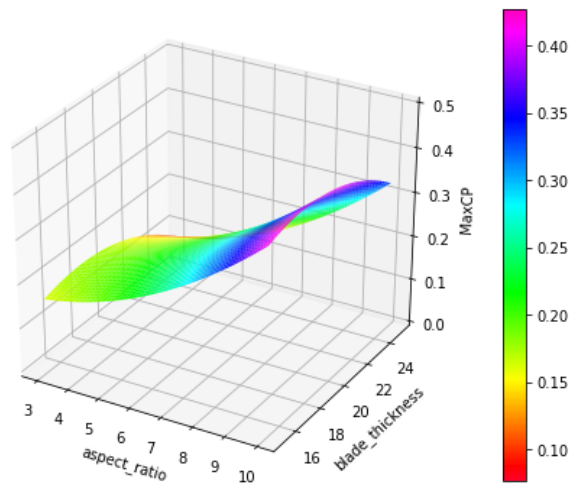


Figure 59 Candidate 3 model equation plane

The model function surface of Candidate 1 is similar to Candidate 2, and has a relatively high correlation to validation cases; however, it only captures the aspect ratio characteristics. As for Candidate 3, it has relatively high coefficient of determination; however, it has the higher difference to validation cases. Although the surface seems to capture the characteristics of both variables, the predicted MaxCP is totally smaller than the other candidates.

5.6 Findings for model functions

We observe the difference between the function and CFD results and conclude:

- Model equations are suggested based on simple regression methods;
- Single function models show a monotonous increase in MaxCP vs Aspect Ratio and a monotonous decrease in MaxCP vs blade thickness;
- Three multiple function models are suggested. Candidate 2 provides reasonable results. It contains one constant, two linear terms and a bilinear term on the Aspect Ratio and blade thickness variables;
- The optimum combination to maximize the MaxCP appears to be the highest Aspect Ratio and the smallest blade thickness.

6 Conclusion

6.1 Summary

The investigation of the power coefficient for VAWTs in this thesis is based on computational methods either extracted from literature or performed in this work. After gathering 28 three-dimensional CFD cases from the literature it was decided to recalculate some of these cases. Furthermore, we analyzed these cases and created some novel and simple models.

First, six three-dimensional simulations are conducted for different geometries to enrich the available data. These cases consist of straight symmetric blades, no supportive parts, and the same turbulence model. The common turbulence model is *SST* $k - \omega$, and each mesh around the blade satisfy that $y^+ \sim 1$. The simulations converge well and provide an accurate C_p . At least 10 revolutions are simulated.

Second, based on all the data available it was observed that specific design variable affects the C_p . The data clearly indicates that the blade thickness and the blade aspect ratios are the main geometric parameters of the affect the C_p . It is no surprize that the blade is in fact the most important feature of the turbine, more than its size though large turbines typically perform better.

Third, some model functions are constructed to roughly predict the power coefficient. The functions try to capture the fact that the large aspect ratio provides high power coefficient and a small blade thickness leads to high power coefficient. Using regression analysis, we proposed some types of model functions for the aspect ratio and blade thickness parameters. These models are examined by comparing with some results of three-dimensional CFD simulations.

To conclude, this thesis exploits available three-dimensional simulations from the literature and newly performed simulation to identify the geometric parameters of VAWT that affect the most the power coefficient. This thesis also includes some proposed model functions to predict the $MaxCP$ based on aspect ratio and blade thickness. This work clearly indicates that optimum combination to maximize the $MaxCP$ is to maximize aspect ratio for a blade with small blade thickness.

6.2 Future work

This thesis only tries to model the behavior of the turbine in terms of predicting C_p based on a few parameters with simple methods, because there are only 28 cases. Gathering more than hundreds of cases can allow more sophisticated method such as a neural networking, a machine learning, or a deep learning. We strongly recommend to perform a lot of CFD simulations for different parameters and refine the model. The created model is accurate in the limited situation, so more works are required in this region. As six cases are simulated, it is important to continue to simulate additional three-dimensional cases for finding and refining model functions.

Furthermore, other technics exist to explore the geometric design space for performance improvement of VAWT. Such techniques as the Double multiple stream tube (DMST) model or the Actuator Line Model can be used to explore a design space faster but these techniques are not as accurate as CFD. There may be a benefit to combine both CFD with other techniques to reduce the computational cost [39] [40].

7 References

- [1] G. W. E. COUNCIL, "Wind Power & Green Recovery Hub," [Online]. Available: <https://gwec.net/greenrecovery/>. [Accessed 24 09 2021].
- [2] I. E. Agency, "Global Energy Review 2020," 4 2020. [Online]. Available: chrome-extension://efaidnbnmnibpcjpcglclefindmkaj/viewer.html?pdfurl=https%3A%2F%2Fiea.blob.core.windows.net%2Fassets%2F7e802f6a-0b30-4714-abb1-46f21a7a9530%2FGlobal_Energy_Review_2020.pdf&clen=2126664. [Accessed 24 9 2021].
- [3] F. Castellani, D. Astolfi, M. Peppoloni, F. Natili, D. Buttà and A. Hirschl, "Experimental Vibration Analysis of a Small Scale Vertical Wind Energy System for Residential Use," *mdpi*, 2019.
- [4] A. Betz, "Windmills In The Light of Modern Research," *Technical Memorandums National Advisory Committee For Aeronautics*, vol. 474, 1928.
- [5] Q. Li, T. Maeda, Y. Kamada, J. Murata, K. Shimizu, T. Ogasawara, A. Nakai and T. Kasuya, "Effect of solidity on aerodynamic forces around straight-bladed vertical axis wind turbine by wind tunnel experiments (depending on number of blades)," *Renewable Energy*, 2016.
- [6] G. Naccache and M. Paraschivoiu, "Development of the Dual Vertical Axis Wind Turbine Using Computational Fluid Dynamics," *ASME*, 2017.
- [7] F. R. Menter, "Two-Equation Eddy-Viscosity Turbulence Models for Engineering Applications," *AIAA Journal*, pp. 1598-1605, 1994.
- [8] N. Franchina, O. Kouaissah, G. Persico and M. Savini, "Three-Dimensional CFD Simulation and Experimental Assessment of the Performance of a H-Shape Vertical-Axis Wind Turbine at Design and Off-Design Conditions," *International Journal of Turbomachinery Propulsion and Power*, 2019.
- [9] X. Cai, Y. Zhang, W. Ding and S. Bian, "The aerodynamic performance of H-type darrieus VAWT rotor with and without winglets: CFD simulations," *Energy Sources, Part A: Recovery, Utilization, and Environmental Effects*, 2019.
- [10] G. Bangga, A. Dessoky, T. Lutz and E. Kr€amer, "Improved double-multiple-streamtube approach for H-Darrieus vertical axis wind turbine computations," *Energy*, 2019.
- [11] N. Franchina, G. Persico and M. Savini, "2D-3D Computations of a Vertical Axis Wind Turbine Flow Field: Modeling Issues and Physical Interpretations," *Renewable Energy*, 2018.

- [12] H. F. Lam and H. Y. Peng, "Study of wake characteristics of a vertical axis wind turbine by two-andthree-dimensional computational fluid dynamics simulations," *Renewable Energy*, 2016.
- [13] H. Lei, D. Zhou, J. Lu, C. Chen, Z. Han and Y. Bao, "The impact of pitch motion of a platform on the aerodynamic performance of a floating vertical axis wind turbine," *Energy*, vol. 119, pp. 369-383, 2017.
- [14] A. Alaimo, A. Esposito,, A. Messineo,, C. Orlando and D. Tumino, "3D CFD Analysis of a Vertical Axis Wind Turbine," *Energies*, vol. 8, pp. 3013-3033, 2015.
- [15] H. Lei, D. Zhou, Y. Bao, Y. Li and Z. Han, "Three-dimensional Improved Delayed Detached Eddy Simulation of a two-bladed vertical axis wind turbine," *Energy Conversion and Management* , vol. 133, pp. 235-248, 2017.
- [16] Y. Hara, N. Horita, S. Yoshida, H. Akimoto and T. Sumi, "Numerical Analysis of Effects of Arms with Different Cross-Sections on Straight-Bladed Vertical Axis Wind Turbine," *Energies*, vol. 12, 2019.
- [17] C. Liang and H. Li, "Effects of optimized airfoil on vertical axis wind turbine aerodynamic performance," *Journal of the Brazilian Society of Mechanical Sciences and Engineering*, 2018.
- [18] T. Q. Le, K.-S. Lee, J.-S. Park and J. H. Ko, "Flow-driven rotor simulation of vertical axis tidal turbines: A comparison of helical and straight blades," *IJNAOE*, vol. 6, pp. 257-268, 2014.
- [19] N. Franchina, G. Persico and M. Savini, "Three-dimensional unsteady aerodynamics of a H-shaped vertical axis wind turbine over the full operating range," *Journal of Wind Engineering & Industrial Aerodynamics*, vol. 206, 2020.
- [20] N. Qin, R. Howell, N. Durrani, K. Hamada and T. Smith, "Unsteady Flow Simulation and Dynamic Stall Behaviour of Vertical Axis Wind Turbine Blades," *WIND ENGINEERING*, vol. 35, no. 511-510, p. 35, 2011.
- [21] C. Liang, D. Xi, S. Zhang and Q. Yang, "Effects of Solidity on Aerodynamic Performance of H-Type Vertical Axis Wind Turbine," *2nd International Symposium on Resource Exploration and Environmental Science IOP Conf. Series: Earth and Environmental Science*, vol. 170, 2018.
- [22] M. Elkhoury, T. Kiwata and E. Aoun, "Experimental and numerical investigation of a three-dimensional vertical-axis wind turbine with variable-pitch," *Journal of Wind Engineering and Industrial Aerodynamics*, vol. 139, pp. 111-123, 2015.

- [23] R. Howell, N. Qin, J. Edwards and N. Durrani, "Wind tunnel and numerical study of a small vertical axis wind turbine," *Renewable Energy*, vol. 35, pp. 412-422, 2010.
- [24] L. X. Zhang, Y. B. Linang, X. H. Liu, Q. F. Jiao and J. Guo, "Aerodynamic Performance Prediction of Straight-Bladed Vertical Axis Wind Turbine Based on CFD," *Advances in Mechanical Engineering*, 2013.
- [25] H. Lei, J. Su, Y. Bao, Y. Chen, Z. Han and D. Zhou, "Investigation of wake characteristics for the offshore floating vertical axis wind turbines in pitch and surge motions of platforms," *Energy*, vol. 166, pp. 471-489, 2019.
- [26] D. A. Dekterev, A. A. Dekterev, A. S. Lobasov, D. V. Platonov, A. V. Sentyabov and A. A. Dekterev, "Simulation of orthogonal rotors with dynamic pitching blades," *Journal of Physics: Conference Series*, 2019.
- [27] N. Ma, H. Lei, Z. Han, D. Zhou, Y. Bao, K. Zhang, L. Zhou and C. Chen, "Airfoil optimization to improve power performance of a high-solidity vertical axis wind turbine at a moderate tip speed ratio," *Energy*, vol. 150, pp. 236-252, 2018.
- [28] Y. Jiang, P. Zhao, T. Stoesser, K. Wang and L. Zou, "Experimental and numerical investigation of twin vertical axis wind turbines with a deflector," *Energy Conversion and Management*, vol. 209, 2020.
- [29] S. Ali, S.-M. Lee and C.-M. Jang, "Effects of instantaneous tangential velocity on the aerodynamic performance of an H-Darrieus wind turbine," *Energy Conversion and Management*, vol. 171, pp. 1322-1338, 2018.
- [30] Z. Wang and M. Zhuang, "Leading-edge serrations for performance improvement on a vertical-axis wind turbine at low tip-speed-ratios," *Applied Energy*, vol. 208, pp. 1184-1197, 2017.
- [31] L. Daróczy, G. Janiga and D. Thévenin, "Optimization of a winglet for improving the performance of an H-Darrieus turbine using CFD," in *International Symposium on Transport Phenomena and Dynamics of Rotating Machinery*, Hawaii, Honolulu, 2016.
- [32] S. H. Hezaveh, E. Bou-Zeid, M. W. Lohry and L. Martinelli, "Simulation and wake analysis of a single vertical axis wind turbine," *Wind energy*, vol. 20, pp. 713-730, 2017.
- [33] K. Souraissa, M. Ghiss, M. Chrigui, H. Bentaher and A. Maalej, "A comprehensive analysis of aerodynamic flow around H-Darrieus rotor with camber-bladed profile," *Wind Engineering*, vol. 43, no. 5, pp. 459-475, 2019.
- [34] A. Subramanian, S. A. Yogesh, H. Sivanandan, A. Giri, M. Vasudevan, V. Mugundhan and R. V. Kishore, "Effect of airfoil and solidity on performance of small scale vertical axis wind turbine using three dimensional CFD model," *Energy* 133, 2017.

- [35] Seimens Product Lifecycle Management Software Inc., *STAR-CCM+ 12.06.011 User Guide*, 2017.
- [36] I. E. Barton, "Comparioson of SIMPLE and PISO Type Algorithms for Transient Flows," *Ineternational Journal for Numerical Methods in Fluids*, pp. 459-483, 1998.
- [37] D. C. Wilcox, *Turbulence Modeling for CFD 2nd edition*, DCW Industries, Inc., 1998.
- [38] P. A. Durbine, "On the k-e stagnation point anomaly," *Int. J. Heat and Fluid Flow*, vol. 17, pp. 89-90, 1996.
- [39] I. Paraschivoiu, *Wind Turbine Design With Emphasis on Darrieus Concept*, Polytechnic International Press, 2002.
- [40] J. N. Sørensen and Wen Zhong Shen, "Numerical Modeling of Wind Turbine Wakes," *Journal of Fluids Engineering*, vol. 124, no. 2, pp. 393-399, 2002.
- [41] Q. Li, T. Maeda, Y. Kamada, J. Murata, K. Shimizu, T. Ogasawara, A. Nakai and T. Kasuya, "Effect of solidity on aerodynamic forces around straight-bladed vertical axis wind turbine by wind tunnel experiments (depending on number of blades)," *Renewable Energy*, vol. 96, pp. 928-939, 2016.
- [42] A. Subramanian, S. A. Yogesh, H. Sivanandan, A. Giri, M. Vasudevan, V. Mugundhan and R. K. Velamati, "Effect of airfoil and solidity on performance of small scale vertical axis wind turbine using three dimensional CFD model," *Energy*, vol. 133, pp. 179-190, 2017.
- [43] M. W. Lohry and L. Mrtinelli, "Unsteady Reynolds-Averaged Navier–Stokes Simulation of Crossflow Rotors, Scaling, and Blockage Effects," *AIAA Journal*, vol. 54, no. 12, pp. 3828-3839, 2016.